

# Contents

<b>1 Gravitational Lensing</b>	<b>3</b>
1.1 Theory of gravitational lensing . . . . .	3
1.1.1 Light deflection according to Newton . . . . .	3
1.1.2 Light deflection according to General Relativity . . . . .	5
1.1.3 The lens equation . . . . .	6
1.1.4 General lensing solution . . . . .	7
1.1.5 Lensing at the first order: the linear solution . . . . .	7
1.1.6 Lensing at the first order: magnification, caustics, critics . . . . .	8
1.1.7 Real strong lenses . . . . .	9
1.2 Lensing applied . . . . .	10
1.2.1 Mass distribution in galaxy clusters . . . . .	10
1.2.2 Galaxy clusters as means to the background source . . . . .	10
1.2.3 Galaxy-galaxy strong lensing . . . . .	11
1.2.4 Map the lens mass distribution . . . . .	11
1.2.5 The fraction of strongly lensed objects at high- $z$ . . . . .	12
1.2.6 Time delays . . . . .	13
1.2.7 Microlensing . . . . .	14
1.2.8 Weak lensing and Large Scale Structure . . . . .	15
<b>2 The fate of the diffuse baryons</b>	<b>17</b>
2.1 The Dark Ages . . . . .	17
2.2 The reionization era . . . . .	18
2.2.1 The Gunn-Peterson effect . . . . .	18
2.2.2 The first light sources in the universe . . . . .	20
2.2.3 The reionization process . . . . .	21
2.3 The Intergalactic Medium . . . . .	22
2.3.1 The Ly $\alpha$ forest . . . . .	22
2.3.2 Absorption systems classification . . . . .	24
2.3.3 The cosmological UV background . . . . .	25
2.3.4 Model for the reionization of the universe . . . . .	25
2.4 The global baryon budget in absorption-line systems . . . . .	26
<b>3 Galaxy formation and evolution</b>	<b>28</b>
3.1 Selection . . . . .	28
3.2 Redshift-distance . . . . .	28
3.2.1 Narrow band technique . . . . .	29
3.2.2 Lyman Break galaxies . . . . .	29
3.2.3 Photometric redshift . . . . .	31
3.3 Physical properties at zero redshift . . . . .	32
3.3.1 Stellar population synthesis . . . . .	32
3.3.2 Initial mass function . . . . .	32
3.3.3 Single stellar populations . . . . .	33
3.3.4 Composite stellar populations . . . . .	33
3.3.5 The spectra of galaxies . . . . .	34
3.3.6 ISM components . . . . .	35
3.3.7 Morphology . . . . .	35
3.3.8 Dynamics . . . . .	36
3.4 Physical properties at high redshift . . . . .	36

3.4.1	Morphology . . . . .	36
3.4.2	Star formation . . . . .	37
3.4.3	Galaxy luminosity function . . . . .	37
3.4.4	Evolution of the mass function . . . . .	38
3.5	Super massive black holes . . . . .	38
<b>A</b>	<b>Lyman-<math>\alpha</math> based techniques</b>	<b>39</b>
A.1	Damped Lyman- $\alpha$ systems (DLA) . . . . .	39
A.2	Lyman- $\alpha$ emitters and blobs (LAEs) . . . . .	39
A.2.1	Lyman- $\alpha$ blobs . . . . .	40

# Chapter 1

## Gravitational Lensing

### 1.1 Theory of gravitational lensing

The idea that gravity deflect light is old. In the 18th century, Michell and Laplace theorized that the mass of a star could be measured from how much the light slows down in its proximity. Cavendish and Soldner actually did the math using newtonian gravity and found that the deflection angle is:

$$\hat{\alpha}(R) = \frac{2GM}{c^2 R} \quad (1.1)$$

that for the Sun assumes a value of  $0.875''$ .

Everything changed after 1915 with the publication of Einstein's Theory of General Relativity. With the new formalism he predicted that a point source with radius  $R$  and mass  $M$  would deflect the light of a background object with a deflection angle of:

$$\hat{\alpha}(R) = \frac{4GM}{c^2 R} \quad (1.2)$$

that for the Sun gives a value  $\sim 1.75$ .

Gravitational lensing played a fundamental role in showing that Einstein's General Relativity is true: Eddington found, during a solar eclipse that the deflection angle for the sun was  $1.60 \pm 0.31$  arcsec, in spectacular accord with what Einstein predicted.

Observing gravitational lensing phenomena has been impossible for decades due to the insufficient instrumentation and the need of pure observations. However theoretical studies on gravitational lensing kept going starting from Chwolson and Einstein that theorized Einstein's rings, till Refsdal who in 1964 discussed on multiple images, magnification, time delays and theorized lensed SNe.

The first gravitational lensing event to be detected was the so-called "twin quasar" in 1979: it basically consists in two quasars with the exact same spectra separated by some arcseconds. The first observation was done in radio: in this band only the lensed object is visible while if we observe in the optical region we can even see the central galaxy. Then in 1985 the first Einstein's cross was observed, in 1988 the first gravitational arcs, in 1990 the first weak lensing detection and in 1993 the first ever microlensing event.

The first systematic lensing surveys in the optical/near-IR are no older than the 2000s, while the ones in sub-mm are around the 2010s.

Observing in the sub-mm allows us to see only the lensed arcs since usually the lens is a massive elliptical galaxy without gas that, for this reason, does not emit in the sub-mm so we have no contamination coming from the lens.

#### 1.1.1 Light deflection according to Newton

According to newtonian gravity, the lensing phenomenon is a simple geometric problem.

Looking at Fig. 1.1 we have a photon with versor  $e_{in}$  going toward the deflector  $M$ , when the versor meets the deflector its versor becomes  $e_{out}$ . The distance between the center of the deflector and the photon is  $r$  and we have  $r^2 = \xi^2 + z^2$  where we call  $\xi$  impact parameter and  $z = ct \rightarrow dz = cdt$ . The deflection angle  $\hat{\alpha} = e_{in} - e_{out}$ .

We know that the force is given by:

$$\vec{F} = -m_\gamma \nabla \phi = m_\gamma \vec{a} \Rightarrow \vec{a} = -\nabla \phi \quad (1.3)$$

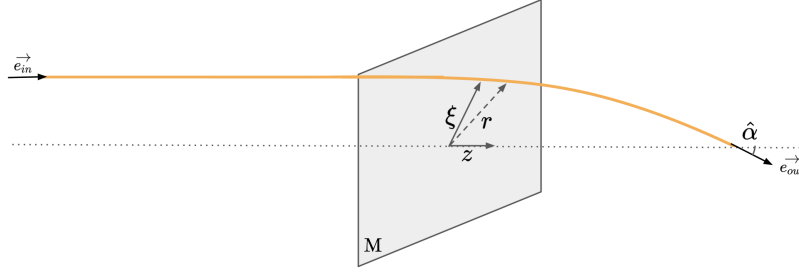


**Figure 1.1:** Scheme of a lens in the newtonian gravity approximation

where

$$\phi = \frac{GM}{r} \quad \text{is the potential} \quad (1.4)$$

As such the photon will experience a change in velocity:

$$\Delta \vec{v} = \int_{t_{in}}^{t_{out}} \vec{a} dt \simeq -\frac{1}{c} \nabla \phi dz \quad (1.5)$$

We can split this change in velocity into parallel and perpendicular component. In this way we have for the parallel component:

$$\Delta v_{\parallel} = -\frac{1}{c} \int_{z_{in}}^{z_{out}} \frac{d\phi}{dz} dz = \frac{1}{c} (\phi_{in} - \phi_{out}) \quad (1.6)$$

We can assume that  $|z_{in}| = |z_{out}| = \infty$  as such  $\phi(\infty) \rightarrow 0 \Rightarrow \Delta v_{\parallel} = 0$  so the velocity in the parallel component remains constant.

For what concerns the perpendicular component we have:

$$\Delta v_{\perp} = \frac{1}{c} \int_{z_{in}}^{z_{out}} \frac{d\phi}{d\xi} dz = -\frac{GM\xi}{c} \int_{z_{in}}^{z_{out}} (\xi^2 + r^2)^{-3/2} dz \quad (1.7)$$

knowing that  $\tan \theta = z/\xi$  we can rewrite

$$\Delta v_{\perp} = -\frac{GM}{c\xi} \int_{-\pi/2}^{\pi/2} \cos \theta d\theta = -\frac{2GM}{c\xi} \quad (1.8)$$

so the photon's velocity will change accordingly in the perpendicular direction.

Therefore:

$$\vec{v}_{out} = |v_{out}| \vec{e}_{out} = c \vec{e}_{in} - \frac{2GM}{c\xi} \vec{e}_{\xi} \quad (1.9)$$

but

$$|v_{out}| = \sqrt{c^2 + \frac{4G^2 M^2}{c^2 \xi^2}} \sim c \quad (1.10)$$

and as such, computing the deflection angle we have:

$$\hat{\alpha} = \vec{e}_{in} - \vec{e}_{out} = \frac{2GM}{c^2 \xi} \vec{e}_{\xi} \quad (1.11)$$

If the impact parameter is  $R_{\odot}$ :

$$\hat{\alpha} = \frac{2GM}{c^2 R_{\odot}} \simeq 0.875'' \quad (1.12)$$

However this is not the right model.

### 1.1.2 Light deflection according to General Relativity

Gravity is a manifestation of spacetime geometry. Matter moves along geodesic but the underlying geometry is curved thus deflect its path from the pure straight-Minkowskian line.

We can study the deflection according to GR treating the problem as in geometrical optics: a refraction problem (change of refractive index). In fact in this model light travels from an unperturbed Minkowski spacetime to a perturbed one (e.g. Schwarzschild). However this does not mean that light actually changes its speed, it means that an external observer sees the action of an effective refraction index that gives the illusion of a speed variation. Let's assume that in the perturbed Schwarzschild metric light travels with speed  $c' = c/n$ .

The metric in the **Minkowski spacetime** is simply:

$$\eta_{\mu\nu} = \begin{pmatrix} 1 & 0 & 0 & 0 \\ 0 & -1 & 0 & 0 \\ 0 & 0 & -1 & 0 \\ 0 & 0 & 0 & -1 \end{pmatrix} \quad (1.13)$$

therefore:

$$ds^2 = \eta_{\mu\nu} dx^\mu dx^\nu = (dx^0)^2 - (d\vec{x})^2 = c^2 dt^2 - (d\vec{x})^2 \quad (1.14)$$

While the metric in the **Schwarzschild spacetime** is:

$$g_{\mu\nu} = \begin{pmatrix} 1 + \frac{2\phi}{c^2} & 0 & 0 & 0 \\ 0 & -(1 + \frac{2\phi}{c^2}) & 0 & 0 \\ 0 & 0 & -(1 + \frac{2\phi}{c^2}) & 0 \\ 0 & 0 & 0 & -(1 + \frac{2\phi}{c^2}) \end{pmatrix} \quad (1.15)$$

and  $ds$  is:

$$ds^2 = g_{\mu\nu} dx^\mu dx^\nu = \left(1 + \frac{2\phi}{c^2}\right) c^2 dt^2 - \left(1 - \frac{2\phi}{c^2}\right) (d\vec{x})^2 \quad (1.16)$$

We know that light propagates with  $ds = 0$  (in the weak field assumption  $\phi/c^2 \ll 1$ ) as such:

$$\begin{aligned} \left(1 + \frac{2\phi}{c^2}\right) c^2 dt^2 &= \left(1 - \frac{2\phi}{c^2}\right) (d\vec{x})^2 \\ \rightarrow c' &= \frac{|d\vec{x}|}{dt} = c \sqrt{\frac{1 + \frac{2\phi}{c^2}}{1 - \frac{2\phi}{c^2}}} \approx c \left(1 + \frac{2\phi}{c^2}\right) \\ \rightarrow n &= \frac{c}{c'} = \frac{1}{1 + \frac{2\phi}{c^2}} \approx 1 - \frac{2\phi}{c^2} \end{aligned} \quad (1.17)$$

Applying the Fermat principle and solving the subsequent Euler-Lagrange equation we obtain:

$$\vec{\alpha} = \int_{\lambda_A}^{\lambda_B} \nabla_{\perp} [\ln(n)] d\lambda \quad (1.18)$$

which tells us that *the deflection always occurs in the perpendicular direction to the light trajectory*.

Since  $\ln(n) \sim -2\phi/c^2$  we find:

$$\vec{\alpha} = \frac{2}{c^2} \int_{\lambda_A}^{\lambda_B} \vec{\nabla}_{\perp} \phi d\lambda \quad (1.19)$$

so *deflection always occurs toward the deflector's center*.

This is the most general expression for the deflection angle, under the assumption of weak field assumption, however it requires an integration over the actual light path. Notice that the deflection angle does not depend on the photon energy: lensing is completely **achromatic**.

To obtain an expression useful in most astrophysical applications let's assume small deflection angles (as expected in weak field) and that the lens mass distribution can be approximated as a flat screen in the context of the full deflection problem.

As such we obtain:

$$\hat{\alpha}(\xi) = \frac{2}{c^2} \int_{-\infty}^{+\infty} \vec{\nabla}_{\perp} \phi(\xi, z) dz \quad \text{for point mass } \phi = -GM \sqrt{\xi^2 + z^2} \quad (1.20)$$

and therefore:

$$\hat{\vec{\alpha}} = \frac{4GM}{c^2\xi} \vec{e}_\xi = \frac{4GM}{c^2\xi^2} \vec{\xi} \quad (1.21)$$

which is just two times the one obtained under Newtonian gravity. Thus if the impact parameter is  $R_\odot$ :

$$\hat{\alpha} = \frac{4GM}{c^2R_\odot} \simeq 1.75'' \quad (1.22)$$

### Different mass distributions

This is for what concerns a point mass. If we are dealing with an **ensemble of point mass** then the total deflection is the sum of every single mass contribution:

$$\vec{\alpha}(\vec{\xi}) = \sum_i^N \vec{\alpha}(\vec{\xi} - \vec{\xi}_i) = \frac{4G}{c^2} \sum_i^N M_i \frac{\vec{\xi} - \vec{\xi}_i}{|\vec{\xi} - \vec{\xi}_i|^2} \quad (1.23)$$

If we are dealing with an **extended mass distribution**, in the thin screen approximation the lens is approximated by a planar distribution of matter. So once defined the lens surface density:

$$\Sigma(\vec{\xi}) = \int \rho(\vec{\xi}, z) dz \quad (1.24)$$

the deflection angle becomes:

$$\vec{\alpha}(\vec{\xi}) = \frac{4M}{c^2} \int \frac{\vec{\xi} - \vec{\xi}'}{|\vec{\xi} - \vec{\xi}'|^2} \Sigma(\vec{\xi}') d^2 \vec{\xi}' \quad (1.25)$$

where  $\xi'$  is the distance at which the light passes with respect to the lens' barycenter (the impact parameter). For a **circularly symmetric mass distribution** we have:

$$\vec{\alpha}(\xi) = \frac{4GM(<\xi)}{c^2\xi} \quad (1.26)$$

with  $M(<\xi) = 2\pi \int d\xi' \xi' \Sigma(\xi')$  which means that only the mass contained within the impact parameter actually enters the deflection angle definition.

### 1.1.3 The lens equation

Consider a simple scheme of a lens, a source and an observer, like the one in Fig. 1.2.

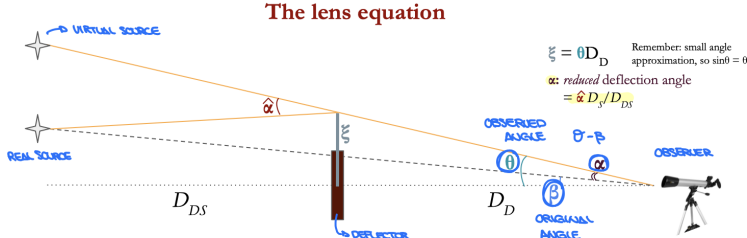


**Figure 1.2:** Simple optical system.

From this scheme is immediately clear that  $\alpha + \beta = \theta$  or, in terms of the segments on the source plane:  $\hat{\alpha}D_{DS} + \beta D_S = \theta D_S$ . If we are working with circularly symmetric lens we have:

$$\beta = \theta - \alpha = \theta - \frac{D_{DS}}{D_S} \hat{\alpha} \quad (1.27)$$

We know that  $\vec{\alpha}(\xi) = 4GM(<\xi)/c^2\xi$  therefore we have:

$$\beta = \theta - \frac{D_{DS}}{D_S} \frac{4GM(\xi)}{\xi c^2} = \theta - \frac{D_{DS}}{D_D D_S} \frac{GM(\theta)}{\theta c^2} \quad (1.28)$$

If we define the **Einstein radius** as:

$$\theta_E = \left( \frac{D_{DS}}{D_D D_S} \frac{4GM(\theta)}{c^2} \right)^{1/2} \quad (1.29)$$

Then we have a second order equation:

$$\beta = \theta - \frac{\theta_E^2}{\theta} \quad (1.30)$$

In case of perfect alignment between the lens and the source ( $\beta = 0$ ) the solution is  $\theta = \theta_E$  and we have the so called **Einstein ring**, otherwise the solution is:

$$\theta_{\pm} = \frac{1}{2} \left( \beta \pm \sqrt{\beta^2 - 4\theta_E^2} \right) \quad (1.31)$$

### 1.1.4 General lensing solution

In the general case of a lens without any particular symmetry (but still in the thin lens hypothesis) the fundamental quantity is the **lensing potential**:

$$\psi(\theta) = \frac{D_{LS}}{D_L D_S} \frac{2}{c^2} \int_{-\infty}^{+\infty} \phi(\xi, z) dz \quad (1.32)$$

The lensing potential satisfies two fundamental properties in gravitational lensing:

$$\begin{aligned} \nabla_{\theta} \psi(\theta) &= \alpha \\ \nabla_{\theta}^2 \psi(\theta) &= 2 \frac{\Sigma(\theta)}{\Sigma^*} = 2K(\theta) \\ \text{with } \Sigma^* &= \frac{c^2}{4\pi G} \frac{D_S}{D_L D_{LS}} \text{ the critical surface density } (\alpha(\theta) = \theta \forall \theta) \end{aligned}$$

The first equation says that **the angular gradient of the lens potential is the reduced deflection angle** while the second one states that **the laplacian of the lensing potential is the convergence K, that is directly related to the lens surface density and therefore to its mass distribution**. Lenses for which  $\Sigma > \Sigma^*$  are said to be *strong lenses*, the opposite case is the one for *weak lenses*.

### 1.1.5 Lensing at the first order: the linear solution

At the first order a lensing phenomena is approximated as a mapping, a transformation between planes: the source plane and the image plane. A mapping between two planes is always obtained from the Jacobian of the transformation  $A = \partial \vec{\beta} / \partial \vec{\theta}$ .

$$A = \partial \vec{\beta} / \partial \vec{\theta} = \delta_{ij} - \frac{\partial \vec{\alpha}}{\partial \vec{\theta}} \quad (1.33)$$

but we have that  $\vec{\alpha} = \frac{\partial \psi}{\partial \vec{\theta}}$  (angular gradient of the lens potential) therefore:

$$A = \delta_{ij} - \frac{\partial^2 \psi}{\partial \theta_i \partial \theta_j} = \delta_{ij} - \Psi_{ij} \quad (1.34)$$

where we define  $\Psi_{ij}$  as the second derivative of the lensing potential, so the gradient field of a gradient field. Remember that  $A$  is a matrix.

Now we split this matrix into two components: the *isotropic* and the *anisotropic* component. The isotropic component is:

$$\frac{1}{2} \text{Tr } A \cdot \mathbb{1} = \left[ 1 - \frac{1}{2}(\Psi_{11} + \Psi_{22}) \right] \delta_{ij} = (1 - K) \delta_{ij} \quad (1.35)$$

from which we state that the convergence is the second derivative of the lensing potential. The anisotropic component is:

$$A - \frac{1}{2} \text{Tr } A \cdot \mathbb{1} = \delta_{ij} - \Psi_{ij} - \frac{1}{2}(2 - \Psi_{11} - \Psi_{22}) \delta_{ij} = \begin{pmatrix} -\frac{1}{2}(\Psi_{11} - \Psi_{22}) & -\Psi_{12} \\ -\Psi_{21} & \frac{1}{2}(\Psi_{11} - \Psi_{22}) \end{pmatrix} \quad (1.36)$$

where  $\frac{1}{2}(\Psi_{11} - \Psi_{22}) = \gamma_1$  and  $\Psi_{12} = \gamma_2$  are the component of a vector called ***shear***.

The mapping we're looking for is then:

$$A = \begin{pmatrix} 1 - K - \gamma_1 & -\gamma_2 \\ -\gamma_2 & 1 - K + \gamma_1 \end{pmatrix} \quad (1.37)$$

The example on Fig. 1.3 shows how the points on the lens/image plane are mapped onto the source plane, once a lens model is assumed.

But what is the meaning of the convergence  $K$  and the shear  $\gamma$ ? Let's consider a simple circular source of radius  $R$  with  $\theta_1^2 + \theta_2^2 = R^2$ :

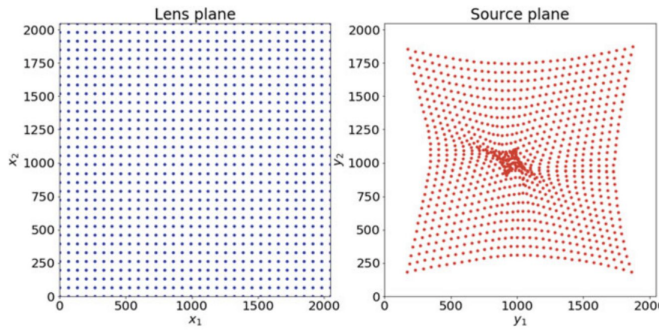


**Figure 1.3:** Example of lensing at the first order using a mapping.

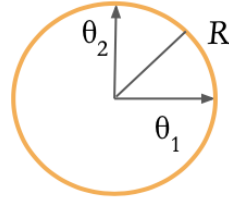


**Figure 1.4:** Circular source

if  $\gamma = 0$  then the matrix becomes:

$$A = \begin{pmatrix} 1 - K & 0 \\ 0 & 1 - K \end{pmatrix} \quad (1.38)$$

so the transformation is:

$$\vec{\beta} = (1 - K)\delta_{ij}\vec{\theta} \Rightarrow (1 - K)^2(\theta_1^2 + \theta_2^2) = R^2 \quad (1.39)$$

so the results is still a circle with radius  $R/(1 - K)$  and since  $K$  is always bigger than 1 the result is a bigger circle. This means that the convergence just increases the size of the source.

Now if we consider the shear:

$$\vec{\beta} = (1 - K)\delta_{ij}\vec{\theta} - \begin{pmatrix} \gamma_1 & \gamma_2 \\ -\gamma_2 & \gamma_1 \end{pmatrix}\vec{\theta} \quad (1.40)$$

the equation becomes the one of an ellipse:

$$(1 - k - \gamma)^2\theta_1^2 + (1 - k + \gamma)^2\theta_2^2 = R^2 \quad (1.41)$$

with:

$$a = \frac{R}{1 - k - \gamma} \quad (1.42)$$

$$b = \frac{R}{1 - k + \gamma} \quad (1.43)$$

The result of the combined action of convergence and shear can be seen in Fig. 1.5. Using more correct terms the convergence term causes an isotropic focusing of light rays, leading to an isotropic magnification of the source while the shear term introduces anisotropy into the lens mapping.

### 1.1.6 Lensing at the first order: magnification, caustics, critics

The surface brightness of a source is defined as:

$$S = \frac{F}{\Omega} = \frac{L}{4\pi A} \quad (1.44)$$

where  $A$  is the area occupied by the source in the source plane. In a lensing phenomena  $S$  remains a constant, therefore if the area  $A$  changes then is necessary that the flux changes proportionally. Considering a full set of multiple images the result is always an increase in  $A$  and therefore a flux magnification. Physically this is motivated by the fact that the observer sees photons that otherwise it would not have seen without the action of the lens.

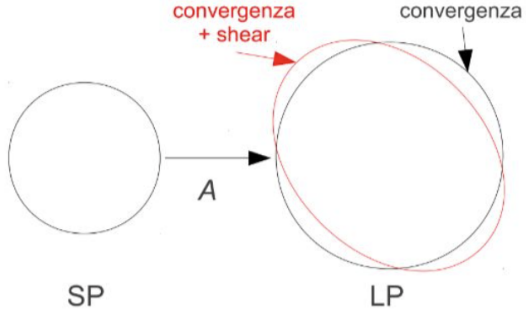


**Figure 1.5:** Combined action of convergence and shear on a circular source.

The magnification is obtained as:

$$\mu = \det M = \frac{1}{\det A} = \frac{1}{(1 - k^2) - \gamma^2} = \frac{\text{image area}}{\text{source area}} = \frac{d\theta^2}{d\beta^2} = \frac{\theta d\theta}{\beta d\beta} \quad (1.45)$$

and the eigenvalues are:

$$\mu_t = \frac{1}{1 - k - \gamma} \quad (1.46)$$

$$\mu_r = \frac{1}{1 - k + \gamma} \quad (1.47)$$

There are points for which  $\mu \rightarrow \infty$  that in the source/image planes define lines called **caustics** and **critics**. The lines of highest magnification in the image plane are called **critics** while the ones in the source plane are called **caustics**.

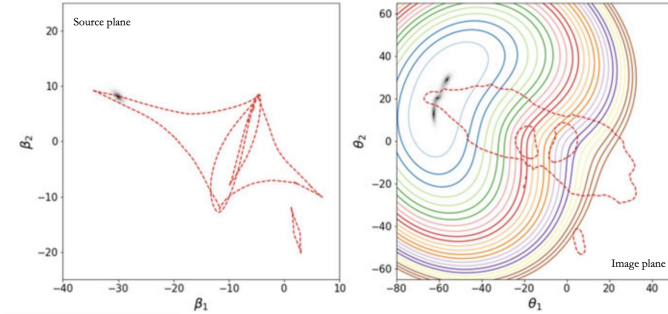


**Figure 1.6:** Critics and caustics

### 1.1.7 Real strong lenses

Let's consider a real lensing application like SDP.9, a source at  $z_s = 1.577$  lensed by a  $z_l = 0.6129$  elliptical galaxy, that in Fig. 1.7 is subtracted to enhance and model the signal from the background source, observed at  $1.6 \mu\text{m}$  with Hubble (unobscured emission of stars) and at  $1.3 \text{ mm}$  with ALMA (emission of dust).

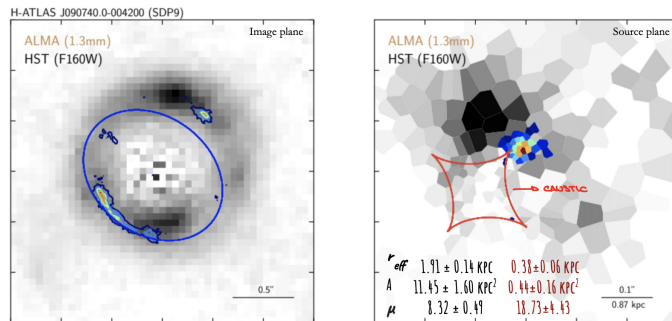


**Figure 1.7:** SDP.9, a strong lensing example

## 1.2 Lensing applied

### 1.2.1 Mass distribution in galaxy clusters

Galaxy clusters are the largest existing virialized objects in the Universe. Their mass distribution can be inferred through kinematic analysis of the member galaxies (virial theorem) or X-ray observations of the hot intracluster medium. Lensing analysis of the whole system is the least model-dependent method (even though we always need a model for the lens) and is the only applicable method for non-virialized clusters.

To see in which scale we are working let's use the Einstein radius previously defined:

$$\theta_E = \left( \frac{D_{DS}}{D_D D_S} \frac{4GM(\theta)}{c^2} \right)^{1/2} \sim 3 \times 10^{-6} \left( \frac{M}{M_\odot} \right)^{1/2} \frac{1}{D_{\text{Gpc}}^{1/2}} \text{arcsec} \quad (1.48)$$

which is of the order of tens of arcsec for a typical galaxy cluster with  $10^{15}$  solar masses.

Let's consider a relaxed and regular galaxy cluster, which is in practice an isothermal self-gravitating gas sphere. That means that the kinetic energy of the particles is constant through the cluster therefore the velocity distribution is Maxwellian  $\Rightarrow kT = \mu \langle v^2 \rangle$ .

The density profile of the cluster can be described as  $\rho(r) = \frac{K_0}{r^2}$  with  $K_0 = \frac{kT}{4\pi G \mu}$  but this is not valid for small radii, where  $\rho$  decreases slower with  $r$  starting at values corresponding to the cluster core radius, and gets to infinity at  $r \rightarrow 0$ ; however is a good approximation in most of the cluster volume.

The constant  $K_0$  can be rewritten in terms of the velocity:

$$K_0 = \frac{kT}{4\pi G \mu} = \frac{\langle v_{\parallel}^2 \rangle}{4\pi G} \quad (1.49)$$

and integrating  $\rho(r)$  we obtain the projected surface mass density (with  $p$  being the impact parameter so the minimum distance between the position of the source and the center of the cluster):

$$\Sigma(p) = \frac{\langle v_{\parallel}^2 \rangle}{4Gp} \quad (1.50)$$

and the mass within the impact parameter becomes:

$$M(< p) = \frac{\pi \langle v_{\parallel}^2 \rangle p}{4G} \quad (1.51)$$

so the deflection angle becomes:

$$\hat{\alpha} = \frac{\pi \langle v_{\parallel}^2 \rangle^{1/2}}{c^2} \sim 6 \left[ \frac{\langle v_{\parallel}^2 \rangle^{1/2}}{1000 \text{ km/s}} \right] \text{arcsec} \quad (1.52)$$

As we see from Eq. 1.52 the deflection angle is independent from  $\rho$ .

But how can we effectively measure the mass distribution using lensing? As always there are two approaches: the parametric one and the free-form one (non-parametric).

In the parametric method we consider three potentials:  $\phi_{\text{smooth}}(\vec{p})$  is the one that traces the gas,  $\phi_{BCG}(\vec{q})$  is the potential of the brightest galaxy within the cluster and  $\phi_{gal}(\vec{s})$  is the potential of all the galaxies of the cluster. Knowing that light traces mass we can derive the mass of the cluster.

On the other hand, if we use the free-form method we make no assumption that light traces mass or on the shape of the density profiles, we simply decompose the cluster into pixels or Radial Basis Functions, each pixel has its own mass distribution and contributes in deflecting the background galaxies' light.

In both these method the best fit is found using Bayesian statistic by maximizing the posteriors.

### 1.2.2 Galaxy clusters as means to the background source

We can focus on the lens, as we have done before, but we can even focus on the source and take advantage of the presence of the lens and of the magnification of the source to study this one more in detail. To do so we need to reconstruct the lensed source, as shown in Fig. 1.8.

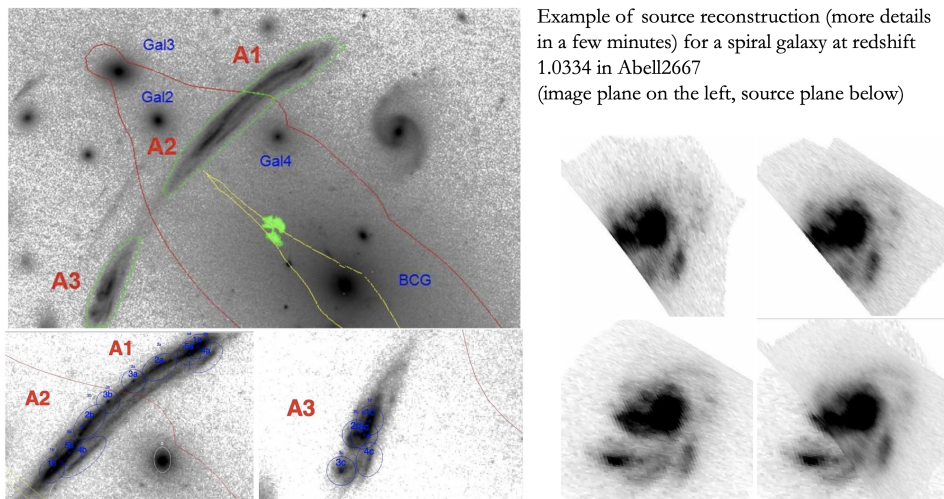


Figure 1.8

### 1.2.3 Galaxy-galaxy strong lensing

The galaxy-galaxy strong lensing is easier to model than other kinds of lensing. In this case we have a nice alignment between two galaxies, usually the foreground galaxy is an elliptical while the magnified one is a spiral. This lensing is important for the building of the Madau plot and therefore for the understanding of the star formation rate. At the cosmic noon (10 Gyr, peak of the Madau plot) we are in a dust-obscured environment so we need to observe in the sub-mm. If we analyze the probability of strong lensing we see that the maximum probability is around  $z = 3$  so exactly at the cosmic noon. Therefore these dust-obscured galaxies (DOGs) are the key to understand the build-up of galaxies.

As we already know in galaxy-galaxy strong lensing we have a natural magnification  $\mu$  so an increased apparent luminosity ( $\sim \mu$ ) and an increased spatial resolution ( $\sim \mu^{1/2}$ ).

How does it work? We have two main components: the lens and the source. For what regards the lens we have to find the lens mass distribution model, which is described by a set of parameters. For example we can consider a **Singular Isothermal Ellipsoid** which is made up of 20% dark matter and 80% light and is described by its velocity dispersion, its axis ratio  $q$  and its position angle  $\theta_{rot}$ .

When dealing with the source we have two approaches: the fully-parametric and the semi-parametric. In the fully-parametric we have that even the source is modeled with an analytical model, like a Sérsic profile while in the semi-parametric approach the source is defined as a grid of pixels/tassels, so its morphology is free to vary.

A strong gravitational lens can reveal fine details of sources in the distant universe. Proper lens modeling and source reconstruction is needed to reconstruct the original source morphology and fully exploit the lens magnification.

### 1.2.4 Map the lens mass distribution

Being lensing a consequence of the presence of matter when we perform lens modeling we have a direct access on how matter is distributed in a galaxy (at least within the Einstein radius). These studies found that the sum of DM and baryonic mass in elliptical galaxies is always an isothermal profile ( $\rho \propto r^{-2}$ ) despite different physical and environmental starting conditions.

Also there is some evidence for a mild evolution of the mass-density slope in ETGs with redshift. Anyway lensing is a powerful key for galaxy evolution and cosmic structure formation.

Also, strong lensing is able to answer the famous "missing satellite problem". The presence of DM substructures is the smoking gun for cosmological models such as  $\Lambda$ CDM, and characterizing their distribution can wipe out lots of theoretical models.

### 1.2.5 The fraction of strongly lensed objects at high- $z$

What is the probability to obtain a strong lensing event along a generic line of sight? The answer is given by the integral of the number density of lenses  $n(z)$  times the strong lensing cross section  $\sigma$ :

$$P(z) = \int_0^z n(z')\sigma(z')dr_{\text{prop}}(z') \quad (1.53)$$

also viewed in terms of **lensing optical depth**  $\tau(z)$  (fraction of sky covered with Einstein rings so how much of the sky is lensed).

Let's take the cross section corresponding to the Einstein radius  $\theta_E$ :

$$\sigma = \pi R^2 = \pi(\theta_E D_D)^2 = \frac{4\pi GM}{c^2} \frac{D_D D_{DS}}{D_S} \quad (1.54)$$

the distance peaks when  $D_D = D_{DS}$  so when the lens is halfway between the source and the observer.

We have then that the maximal lensing probability happens for lenses falling between  $z \sim 0.3 - 1$  and sources at  $z \sim 1 - 3$ .

In the end:

$$\tau(z) = P(z) \sim \frac{3\Omega_D}{2} \int_0^{z_s} \frac{d_D d_{DS}}{d_S} \frac{1+z}{\sqrt{1+\Omega_z}} dz \quad (1.55)$$

where  $d_D = H_0 D_D / c$  and similarly for  $d_S$  and  $d_{DS}$ .

For  $\Omega = 1$  and  $z_s = 3$ , considering that  $d_D d_{DS} / d_S \sim 1$  we have:

$$\tau(z_s = 3) \sim 0.5\Omega_D \quad (1.56)$$

where  $\Omega_D$  is the cosmological parameter of lenses so the density of lenses in the universe.

The most effective lensing structures are galaxies' cores (early type, massive elliptical ones). We can then say that:

$$\Omega_D \sim 10^{-1}\Omega_{gal} \sim 10^{-3} \quad (1.57)$$

so for generic sources at redshift 3, roughly one out of  $10^3 - 10^4$  high-z quasars are strongly lensed, for typical cosmological parameters.

A deeper quantitative analysis requires a more precise evaluation of the strong lensing probability as a function of the angular distance between the source and the lens. For example let's consider point mass lenses with:

$$\theta_{\pm} = \frac{1}{2} \left( \beta \pm \sqrt{\beta^2 - 4\Theta_E^2} \right) \quad (1.58)$$

and with magnification:

$$\mu(x) = \frac{x^2 + 2}{x\sqrt{x^2 + 4}} \quad \text{with} \quad x = \beta/\theta_E \quad (1.59)$$

$x$  can be seen as how many Einstein radius is the source distant from the center of the lens.

Now let's compute the lensing cross-section as a function of the flux amplification. The lensing cross-section is the proper area around a given lens through which the un-deflected light ray would need to pass to cause an amplification greater than  $\mu$ .

$$\sigma(>\mu) = \pi[D_D \beta(\mu)]^2 \quad (1.60)$$

with  $\beta(\mu)$  being the source undeflected angle on the sky within which the amplification is larger than  $\mu$ ,

$$\beta^2 = 2\theta_E^2 \frac{\mu - \sqrt{\mu^2 - 1}}{\sqrt{\mu^2 - 1}} \Rightarrow \sigma(>\mu) = \frac{8\pi GM}{c^2} \frac{D_D D_{DS}}{D_S} \frac{1}{\mu^2 + 1 + \mu\sqrt{\mu^2 - 1}} \propto \mu^{-2} \quad (1.61)$$

On the other hand if we assume an isothermal sphere we obtain:

$$\begin{aligned} \sigma(>\mu) &= \left[ \frac{4\pi G \langle v_{||}^2 \rangle}{c^2} \right]^2 \left( \frac{D_D D_{DS}}{D_S} \right)^2 \frac{4\pi}{\mu^2} \quad \text{if } \mu > 2 \\ \sigma(>\mu) &= \left[ \frac{4\pi G \langle v_{||}^2 \rangle}{c^2} \right]^2 \left( \frac{D_D D_{DS}}{D_S} \right)^2 \frac{\pi}{(\mu - 1)^2} \quad \text{if } \mu < 2 \end{aligned} \quad (1.62)$$

The probability to obtain a strong lensing event along an arbitrary line of sight with amplification  $> \mu$  is:

$$P(z) = \int_0^z n(z') \sigma(> \mu, z') dr_{\text{prop}}(z') \propto \mu^{-2} \quad (1.63)$$

This of course depends also on other cosmological or population parameters, in particular  $\Omega_m$  and  $\Omega_\Lambda$ .

Cosmic Lens All Sky Survey (CLASS) is a radio survey with the Very Large Array, Very Long Baseline Array and MERLIN. They found a ratio of lensed:unlensed radio sources of one per  $690 \pm 190$  targets consistent with  $\Omega_\Lambda + \Omega_m = 1$  (flat universe) and leading to:

$$\Omega_\Lambda = 0.69^{+0.31}_{-0.24} \quad (1.64)$$

Note that we have big errors but the trust value is consistent.

### 1.2.6 Time delays

The deflection of light always causes a delay in the travel time of light between the source and the observer. This time delay has two components:

$$\Delta t = \Delta t_{\text{grav}} + \Delta t_{\text{geom}} \quad (1.65)$$

where  $\Delta t_{\text{grav}}$  is the **Shapiro time delay** caused by the fact that light that travels from Minkowskian to Schwarzschild metric seems to slow down, while  $\Delta t_{\text{geom}}$  is the **geometric delay** which depends on the lenght of the path.

We have:

$$c\Delta t_{\text{grav}} = - \int (1+z_D) \frac{2\phi}{2} dl \quad (1.66)$$

$$c\Delta t_{\text{geom}} = (1+z_D) \frac{D_D D_S}{D_{DS}} \frac{\alpha^2}{2} \quad (1.67)$$

Both depends on lens specifics (potential, deflection angle) therefore the different multiply lensed images of the same source will be delayed in time and the actual delay depends on the lens and on the cosmology.

$$\Delta t \propto D_{\Delta t} \times \phi_{\text{lens}} \rightarrow D_{\Delta t} \propto 1/H_0 \quad (1.68)$$

where  $D_{\Delta t} = (1+z_D) \frac{D_S D_D}{D_{DS}}$  is the time delay distance. This means that knowing the total time delay that is proportional to the time delay distance multiplied by the potential of the lens we can derive the Hubble constant (independent method).

This method is called **time delay cosmography** and we can see an example in Fig. 1.9. In this figure we have four different lightcurves but they are actually referred to the same quasar which is lensed four times.

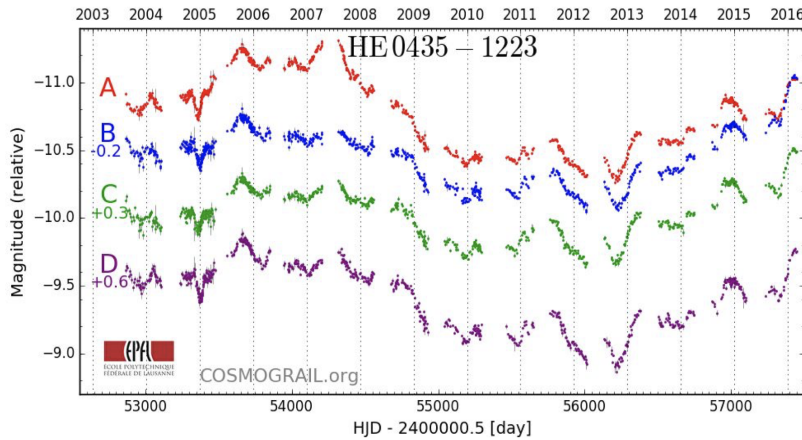


**Figure 1.9:** Time delay cosmography from HoliCow collaboration.

The Hubble constant measured from HoliCow from blind analysis of 4 multiply-imaged quasar systems through strong gravitational lensing is  $H_0 = 72.5^{+2.1}_{-2.3}$  km/s/Mpc, so with a 3% precision in the standard flat  $\Lambda$ CDM model.

### 1.2.7 Microlensing

We talk about microlensing when the spatial resolution is not enough to resolve the lensing features (basically a strong lensing event but at low resolution) so we can just observe a flux magnification with an unique light-curve shape. The angular scale we are working with is:

$$\theta_E = \left( \frac{D_{DS}}{D_D D_S} \frac{4GM(\theta)}{c^2} \right)^{1/2} \sim 0.3 \cdot 10^{-3} \left( \frac{M}{M_\odot} \right)^{1/2} \left( \frac{D'}{10 \text{ kpc}} \right)^{1/2} \text{ arcsec} \quad (1.69)$$

This phenomenon can be used to detect objects with a broad range of masses: planets, stars, star clusters, compact objects in the MW or other galaxies. Historically it was the first method to actually probe if dark matter is made of MAssive Compact Halo Objects (MACHOs).

A microlensing event caused by a transient object has a peculiar light-curve that can be seen in Fig. 1.10.

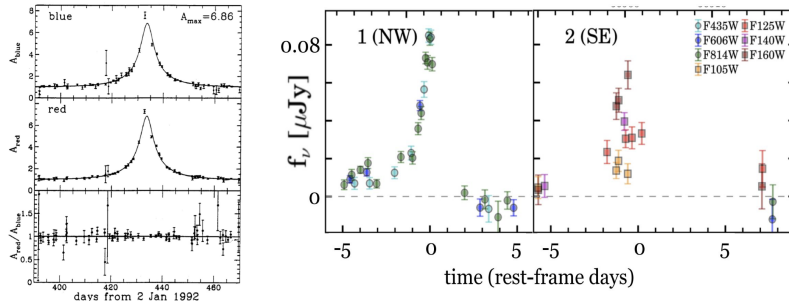


**Figure 1.10:** First detected microlensing event which lasted for about two days

The characteristic timescale for a microlensing event is:

$$\dot{\theta} = \frac{v}{D_D} = 4 \cdot 10^{-3} \left( \frac{v}{200 \text{ km/s}} \right) \left( \frac{D_D}{10 \text{ kpc}} \right) \text{ arcsec yr}^{-1} \quad (1.70)$$

and the typical timescale of the flux variation due to the lensing event is:

$$t_E = \frac{\theta_E}{\dot{\theta}} = 0.2 \left( \frac{M}{M_\odot} \right)^{1/2} \left( \frac{v}{200 \text{ km/s}} \right)^{-1} \left( \frac{D_D}{10 \text{ kpc}} \right)^{1/2} \left( 1 - \frac{D_D}{D_S} \right)^{1/2} \text{ yr} \quad (1.71)$$

which is a couple of days for typical parameters values. Finally the microlensing cross section is directly related to the Einstein ring as:

$$\sigma_{\text{micro}} = \pi \theta_E^2 \quad (1.72)$$

The main problem is that there are billions of reasons for which a star could change its flux, all linked with their intrinsic variability or to environmental effects. However we have two main things that discriminate between a microlensing event and another phenomenon:

- lensing is **achromatic**: if the same flux variability is detected in multiple bands is a clear indication that there is a microlensing event;
- microlensing light-curve has an unique shape, is symmetric with respect to the maximum and is, once again, achromatic.

Imagine having a foreground lens and a moving background source moving along a straight line, like in Fig. 1.11:  $y_0$  is the normalized impact parameter in unit of  $\theta_E$  which is the closest lens-source distance at time  $t_0$ .

The source trajectory is:

$$y(t) = (y_0^2 + y_1^2(t))^{1/2} = \left( y_0^2 + \frac{\dot{\theta}^2(t-t_0)^2}{\theta_E^2} \right)^{1/2} = \sqrt{y_0^2 + \left( \frac{t-t_0}{t_E} \right)^2} \quad (1.73)$$

The magnification  $\mu$  for a point mass lens is:

$$\mu(y) = \frac{y^2 + 2}{y\sqrt{y^2 + 4}} \quad (1.74)$$

therefore the source flux changes in time as:

$$S(t) = S_0 \times \mu[y(t)] = S_0 \times \frac{y^2 + 2}{y\sqrt{y^2 + 4}} \quad (1.75)$$

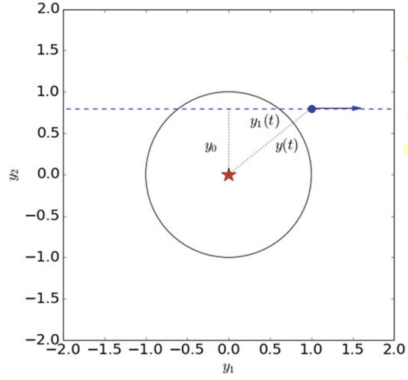


**Figure 1.11:** Microlensing scheme

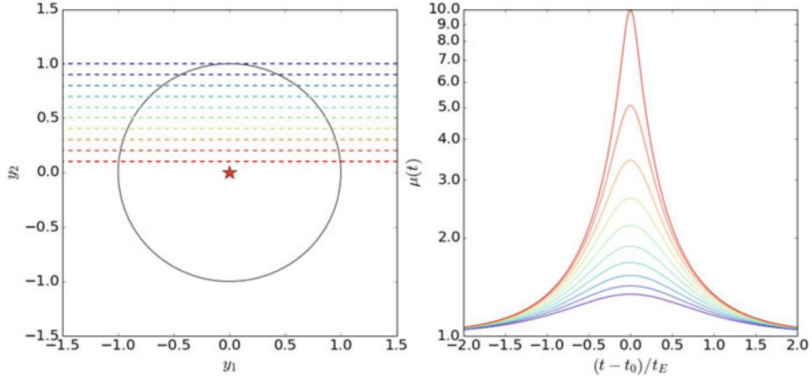


**Figure 1.12:** Microlensing light curve for different  $y_0$ : the bigger the impact parameter, the lower the change in luminosity.

**Microlensing and star masses** As we have just said the source flux variation is given by:

$$S(t) = S_0 \times \mu[y(t)] = S_0 \times \frac{y^2 + 2}{y\sqrt{y^2 + 4}} \quad (1.76)$$

We know everything: the unlensed flux  $S_0$ , the time of the peak  $t_0$ , the smallest distance  $y_0$  and the typical timescale  $t_E$  but this last one is  $t_E \propto \sqrt{MD_D}/v$  and we are not able to disentangle between these three quantities.

This is called *microlensing degeneracy*: one cannot infer the distances, the velocity and the lens mass uniquely from the microlensing light-curve. Of course if one knows two of them from other independent measurement then a microlensing event gives you a way to measure the third one.

**Microlensing and DM: MACHOs** The concept is: if the MW halo is full of MACHOs, those should generate microlensing events in the background objects such as the LMC or the SMC. Therefore the number density of MACHOs would be proportional to the number of microlensing events, and their characteristic mass proportional to the timescale  $t_E$ . The main results are that most microlensing events toward the bulge are most likely caused by known stellar populations and that there are hints at the presence of free-floating planets in the MW disk.

### 1.2.8 Weak lensing and Large Scale Structure

The zero order definition is that strong lensing is when multiple images are generated, weak lensing is when these are not. The lens however is still there and imprints its signature on the shapes and orientation of the background galaxies.

The convergence power spectrum is given by:

$$P_\kappa(l) = \frac{9H_0^4\Omega_{m,0}}{4c^4} \int_0^{w_H} \frac{W^2(w)}{a^2(w)} P_\delta \left( \frac{l}{f_K(w), w} \right) dw \quad (1.77)$$

and depends on cosmology in several ways: it is sensitive to the growth of structures within the universe, to the square of matter density  $\Omega_m$ , to the geometry of the universe in the factor  $f_K$ . This is a measurable quantity, assuming that you are able to accurately map slices of the universe in the whole sky up to high redshift (weak lensing tomography). Of course there are a lot of complications in doing so:

- signal amplitude is tiny (order of 0.01)
- degenerate cosmological parameters
- systematics to accurately model
- high accuracy in measurements is crucial for the theoretical measurement (sometimes solved using machine learning techniques)

# Chapter 2

## The fate of the diffuse baryons

### 2.1 The Dark Ages

After the recombination at  $z \sim 1000$ , the primeval gas, dominated by the hydrogen and helium, remained mostly neutral for relatively long time. These are the so-called dark ages because no significant radiation source was active until the first objects started to shine.

The range of redshifts between  $z \sim 1000$  and  $z \sim 10$  are very difficult to observe in the optical waveband due to the presence of Lyman- $\alpha$  and Lyman continuum absorption. The only tool to observe in this phase is the **21 cm line of neutral hydrogen**. This line is related to the ground state of the hydrogen exhibiting a hyperfine structure in which the state with parallel spin (triplet) has a slightly higher energy than the state with anti-parallel spin (singlet), therefore the 21 cm line is associated to the transition between these two energy levels of the ground state. Is a forbidden line with a probability of transition of  $\sim 2.85 \cdot 10^{-15} \text{ s}^{-1}$ , one every  $10^7$  years. Despite this low decay rate, this transition occurs quite frequently due to the great amount of hydrogen in the Universe.

Now we need to solve the radiative transfer equation which quantifies the energy carried by the radiation traveling along a given direction. For the 21 cm line intensity the solution of the transfer equation gives:

$$T_b(z) = 27x_{HI}(1 + \Delta_B) \frac{\Omega_B h^2}{0.023} \left( \frac{0.15}{\Omega_m h^2} \frac{1+z}{10} \right)^{1/2} \frac{T_S - T_{CMB}(z)}{T_S} [\text{mK}] \quad (2.1)$$

where  $T_b(z)$  is the brightness temperature,  $\Delta_B = d\rho_B/\rho_B$  is the baryon density,  $x_{HI}$  is the neutral hydrogen fraction,  $T_{CMB}$  is the temperature of the CMB at a given  $z$ .  $T_S$  is the spin temperature of the neutral hydrogen and describes the number density of neutral hydrogen atoms in the 1S singlet and triplet state,  $n_0$  and  $n_1$  respectively, through the expression:

$$\frac{n_1}{n_0} = 3 \exp \left( -\frac{T_{12}}{T_S} \right) , \quad \text{with} , \quad T_{21} = \frac{hc}{k\lambda_{21}} = 0.0628 \text{ K} \quad (2.2)$$

and can be written as the weighted average of  $T_K$  (kinetic temperature of the gas),  $T_{CMB}$  and  $T_{Ly-\alpha}$  (color temperature of the Ly- $\alpha$  radiation field). While the radiation and matter are strongly coupled at  $z \geq 200$  then  $T_S = T_\gamma$  and there is no 21 cm signal.

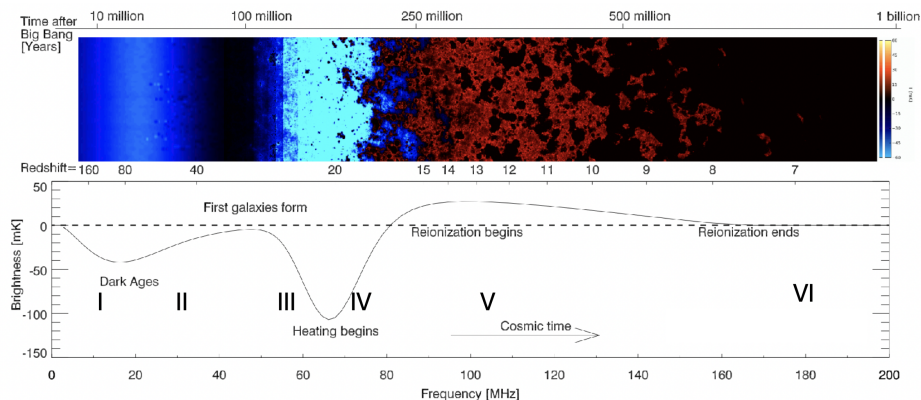


**Figure 2.1:** Expected evolution of the brightness temperature of the 21 cm line normalized to that of the CMB. Roman numbers refer to the different evolutionary phases.

Once the matter and radiation decouple the kinetic temperature drops below the temperature of the background radiation  $T_K < T_\gamma$  at sufficiently low redshift and so the 21 cm line would be seen in absorption against the background radiation in regions of maximum density. Once the heating of neutral hydrogen elevated the temperature of the gas above that of the background radiation the 21 cm line would be expected to be observed in emission.

The different evolutionary phases of HI shown in Fig. 2.1 are:

- I HI is colder than radiation ( $T_S = T_K < T_{CMB}$ ) because gas cools faster than radiation but there is enough gas density to keep spin and kinetic temperature equal.
- II The universe expands and the temperature decouple because the collisions are no more effective and we get  $T_K < T_S < T_{CMB}$  because the spin temperature feels more the CMB photon bath and less the kinetic.
- III First luminous sources produce tiny Ly- $\alpha$  background heating up the gas, there is a recoupling of  $T_S$  and  $T_K$  via the resonant scattering of the Ly- $\alpha$  photons and this produces strong absorption,  $T_K \approx T_S \ll T_{CMB}$ .
- IV Ly- $\alpha$  becomes more intense and heats up the gas.
- V Hotter and hotter gas is observable in emission above the CMB intensity, both the  $T_S$  and the  $T_K$  exceed the CMB temperature. however at lower redshift the reionization increases, neutral hydrogen is removed and the spin temperature decreases approaching the zero.

The main experimental challenges are that the signal is tiny, of the order of mK, and we have a strong foreground signal (synchrotron from MW, free-free in the ISM) that luckily are featureless. In any case the signal is searched as excess or deficit against the foreground.

Thanks to radio telescopes arrays at low radio frequencies is possible to identify not only the spectral emission and absorption signals of the 21 cm line along the line of sight but also perform a 3-dimensional spectral mapping hence obtaining a full tomography of the baryon universe (SKA, 2030).

## 2.2 The reionization era

The analysis of the 21 cm and molecular line signals turn out to be particularly interesting in relation to what happened in the proximity of the reionization era, when the baryonic gas started collapsing and the first stars formed during what we call *cosmic dawn*. These first sources of radiation started ionizing the universe and for this reason the cosmic dawn makes a transition between an essentially neutral universe to an essentially largely ionized universe.

### 2.2.1 The Gunn-Peterson effect

The interplay between the ionizing sources and the surrounding intergalactic gas determines the nature of the reionization.

In 1965 Gunn and Peterson first proposed using Ly- $\alpha$  resonance absorption in the spectrum of distant quasars as a probe of the neutral hydrogen density in the IGM at high-redshift: for objects beyond the reionization, neutral hydrogen in the IGM create complete Gunn-Peterson absorption troughs in the quasar spectrum blueward of the Ly- $\alpha$  emission. In order to clarify this effect, an example of a  $z > 6$  quasar spectrum in the observed frame is presented in Fig. 2.2.

Redward of the Ly- $\alpha$  emission line (red-dashed line) a series of metal lines can be seen. At shorter wavelength the Ly- $\alpha$  forest appears, due to the intervening neutral hydrogen along the line of sight, gas that has remained partly neutral due to self-shielding, hence proportional to the cloud column density.

The Gunn-Peterson trough is also evident above 8400 Å. Between the green and orange dashed lines (respectively Ly- $\gamma$  and Ly- $\beta$  transitions) lies the Ly- $\beta$  forest. At even shorter wavelengths, overlapping higher-order Lyman series transitions occur. The blue line marks the Lyman continuum: photons with rest frame wavelength  $\lambda < 912$  Å are energetic enough to photo-ionize hydrogen atoms creating a continuum absorption region.

In lower-redshift quasar spectra, Lyman-Limit systems (LSSs) can be identified in this zone.

We can describe the Gunn-Peterson effect with a physical model. Consider a photon emitted by a distant quasar at redshift  $z_q$  passing through an uniform IFM with proper number density of neutral hydrogen  $n_{HI}$ . Traveling in the expanding universe at some intermediate point between the quasar and the observer, the photon is redshifted to around  $\lambda_0 = 1216$  Å (Lyman- $\alpha$  wavelength) in the rest-frame of the intervening medium. If neutral hydrogen is present, the photon can be absorbed and the Ly- $\alpha$  transition excited (absorbed in the rest-frame of the cloud). An observer will see this light at redshift  $z_C < z_q$  with frequency  $\nu = \nu_\alpha / (1 + z_C)$  where  $\nu_\alpha$  is the Ly- $\alpha$  frequency in the local IGM

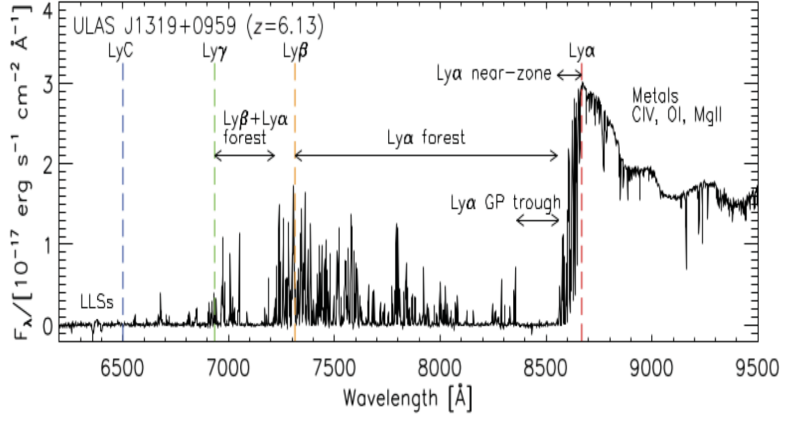


**Figure 2.2:** High signal to noise spectrum of the quasar ULAS J1319+0959 at  $z = 6.13$  which illustrates several key spectral feature used to infer the IGM properties approaching the EoR.

fame.

The optical depth along a particular line of sight from the observer to the quasar is:

$$\tau_{GP}^\alpha = \int_0^{z_q} \sigma[(1+z)] n_{HI}(z) \frac{dl}{dz} dz \quad (2.3)$$

where  $dl/dz = -c/[H(z)(1+z)]$  is the proper line element and  $\sigma$  is the effective scattering cross section. In particular:

$$\sigma[(1+z)] = \frac{\pi e^2}{m_e c} f \phi[\nu(1+z)] \quad (2.4)$$

where  $f = 0.1462$  is the Ly $\alpha$  oscillator strength so the probability of the photon to be absorbed in the transition between the two energy levels and  $\phi$  is the line profile function. Assuming that the Ly $\alpha$  function is basically a delta function centered at frequency  $\nu_\alpha$  and changing the variable of the integration, the optical depth becomes:

$$\tau_{GP}^\alpha = \frac{\pi e^2 f}{H_0 m_e \nu_{Ly\alpha}} \frac{n_{HI}}{(1+z)^{3/2}} \quad (2.5)$$

Now, considering that for a matter dominated universe we have

$$H(z) \simeq H_0 \Omega_m^{1/2} (1+z)^{3/2} \quad (2.6)$$

and that

$$n_{HI} = \frac{\Omega_B \rho_C}{m_H} x_{HI} (1+3)^3 \quad (2.7)$$

the final result will be:

$$\tau_{GP}^\alpha = 5 \cdot 10^5 x_{HI} \frac{\Omega_B h^2}{0.02} \left( \frac{\Omega_m g^2}{0.15} \right)^{-1/2} \left( \frac{1+z}{7} \right)^{3/1} \quad (2.8)$$

Unfortunately even a tiny fraction of neutral hydrogen of the order of  $10^{-5}$  in the IGM could result in a large optical depth and undetectable flux in the Ly forest region.

A more evident signature of the approach to the epoch of reionization is given in Fig. 2.3 that displays the observed redshift evolution of the effective GP optical depth. It is evident that  $\tau_{eff}$  exhibits both a strong overall increase with redshift and an enhanced scatter at  $z > 5$ . The rapid redshift evolution of the optical depth near  $z \sim 6$  may be interpreted as a requirement to complete the reionization at that redshift, however the presence of any transmission at  $z < 6$  could just demands that some regions in the IGM are highly ionized.

In fact, even though a lower limit at  $z \sim 6$  is justified by the detection of flux in the Ly $\alpha$  Gunn-Peterson through quasars, when viewed in the context of a patchy and extremely inhomogeneous reionization, the picture becomes less clear.

As reionization approaches the end, HII regions gradually merge and the remaining neutral patches become increasingly rare and could also have very large sections in the line of sight. Therefore is hard to distinguish in the Ly $\alpha$  statistics, dark patches arising from pre-overlap neutral regions from the dark patches present due to the residual

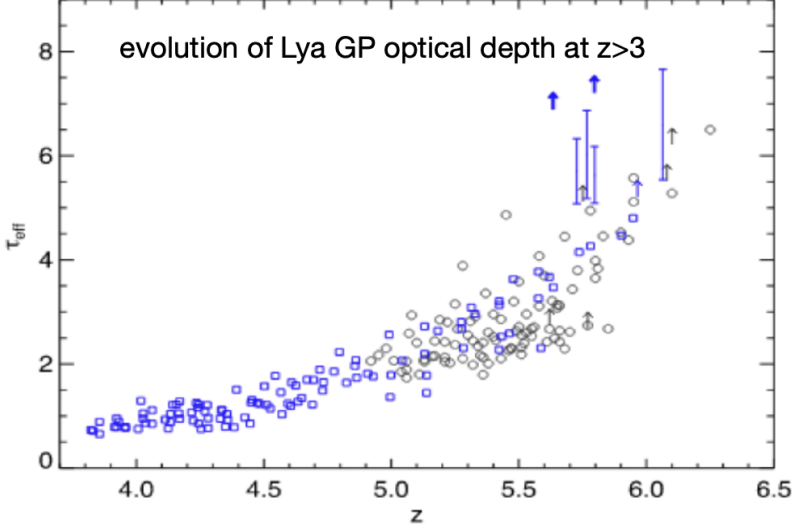


**Figure 2.3:** Evolution of the Gunn-Peterson optical depth with redshift

neutral hydrogen.

In conclusion while the mean Ly $\alpha$  forest transmission indicates that the IGM is highly ionized at  $z < 6$  it is unable to unambiguously determine the duration and the end of the reionization process.

The most precise and less biased estimate of the epoch of reionization so far comes from the highly detailed analysis of the CMB anisotropies. This however does not offer us the details with which the process has taken place. In the future with the already mentioned radio arrays will be possible to make a detailed analysis of the reionization process using the 21 cm tomography.

### 2.2.2 The first light sources in the universe

We know that reionization happened for photoionization and that two main sources may account for the energetic photons that caused it: hot stars or AGNs. Currently is thought that the main source of photoionization photons is the first generation of hot stars. Therefore understanding reionization is directly linked to understanding the first generation of stars.

In the present universe star formation occurs in galaxies thus one need to examine when the first galaxies cold have formed. Two conditions need to be fulfilled for stars to form in dark matter halos: gas needs to be able to fall into the dark halo and it needs to be able to cool, condensing into clouds in which stars can form.

**The Jeans Mass** We consider a slightly overdense spherical region of radius  $R$  whose density is only a little larger than the mean cosmic matter density  $\bar{\rho}$ . If this sphere is homogeneously filled with baryons the gravitational binding energy of the gas is about:

$$|E_{grav}| \sim \frac{GMM_b}{R} \quad (2.9)$$

where  $M$  and  $M_b$  denote the total mass and the baryonic mass of the sphere. The thermal energy can be computed from the kinetic energy:

$$E_{th} \sim c_s^2 M_b \quad (2.10)$$

where

$$c_s \approx \sqrt{\frac{k_B T_b}{\mu m_p}} \quad (2.11)$$

is the speed of sound in the gas, which is about the average speed of the gas particles, and  $\mu m_p$  denotes the average particle mass in the gas. For the gas to be bound in the gravitational field, its gravitational binding energy needs to be larger than the thermal energy which yields to the condition  $GM > c_s^2 R$ . Since we have assumed an only slightly overdense region the relation  $M \sim \bar{\rho} R^3$  between mass and radius of the sphere applies.

From the two latter equations we have:

$$M > \left( \frac{c_s^2}{G} \right)^{3/2} \frac{1}{\sqrt{\bar{\rho}}} \quad (2.12)$$

Thus we find that the mass of the halo needs to exceed a certain threshold for gas to be able to fall in. A more accurate treatment yields the condition:

$$M > M_J = \frac{\pi^{5/2}}{6} \left( \frac{c_s^2}{G} \right)^{3/2} \frac{1}{\sqrt{\rho}} \quad (2.13)$$

where  $M_J$  is the **Jeans mass** which describes the minimum mass of a halo required for the gravitational infall of the gas, expressed through the sound speed and the mean cosmic matter density. The latter can be expressed as a function of the redshift  $\bar{\rho}(z) = \bar{\rho}_0(1+z)^3$ .

For high redshift  $z \geq z_t$  where

$$z_t \approx 140 \left( \frac{\Omega_b h^2}{0.22} \right)^{2/5} \quad (2.14)$$

baryons are coupled with photons via compton scattering, therefore we have an high  $M_J$  and no collapse.

For smaller redshift we have:

$$M_J = 1.35 \cdot 10^5 \left( \frac{\Omega_m h^2}{0.15} \right)^{-0.5} \quad (2.15)$$

and structures can collapse.

**Cooling of the gas** In order to form stars the gas in the halos needs to be cool. In this case we are dealing with the peculiar situation of the first galaxies in which we have no metal so metal lines can't contribute to the cooling process that can only happen via hydrogen and helium.

The first excited state of the hydrogen has a high energy, its cooling effect is efficient only for  $T > 10^4$ , however the first clouds are colder than that. Furthermore helium is completely useless since its excitement temperature is higher than that of the hydrogen.

The only molecule that can provide an efficient cooling is  $H_2$  that, despite its very small transition probability dominates the cooling rate of the primordial gas as temperatures below  $T \sim 10^4$  K. By means of  $H_2$ , the gas can cool in halos with temperature exceeding about  $T_{vir} > 3000$  K, corresponding to a mass of  $M > 10^4 M_\odot$ . In these halos stars are able to form. However these stars are way different from the ones we know since they do not contain metals and therefore the opacity of the stellar plasma is much lower.

These stars are called **Population III stars** and due to their high temperature they are very efficient sources of ionizing photons than stars with normal metallicity.

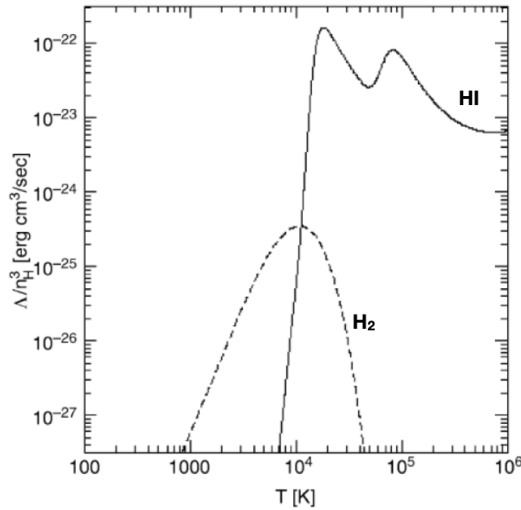


**Figure 2.4:** Cooling rate as a function of the temperature for a gas consisting of atomic and molecular hydrogen and helium. At considerably lower temperature the gas cannot cool, hence no star formation will take place.

### 2.2.3 The reionization process

**Dissociation of molecular hydrogen** Energetic photons from these population III stars are capable of ionizing hydrogen in their vicinity. The binding energy of  $H_2$  is only 11.26 eV, and photons with that energy can propagate for very long distances in the universe. This means that as soon as the first stars have formed in a region of the universe, molecular hydrogen in their vicinities will be destroyed and further star formation will then be prevented.

**Metal enrichment of IGM** Pop III stars then explode as SNe, enriching the IGM with metals that can act as coolant for the next generation of stars (pop II stars)

**Final step of reionization** For gas to cool in halos without molecular hydrogen, their virial temperature needs to exceed about  $10^4$  K. In these halos efficient stellar formation can take place and the first proto-galaxies can form and ionize the IGM in the form of HII regions. These HII regions will expand because increasingly more photons are produced. If the halo density is high enough, these HII regions will start to overlap. Once this occurs the IGM is ionized and reionization is completed.

We can therefore conclude that reionization is a two stage process: in the first phase pop III stars form through cooling of gas by molecular hydrogen which is then destroyed by the same stars. Only in later epoch and in more massive halos the cooling is provided by atomic hydrogen that then leads to reionization.

## 2.3 The Intergalactic Medium

The history of IGM is highly coupled with the cosmic evolution of structure formation. As we have already said the first stars formed and then destroyed with their radiation the molecular hydrogen coolants, shutting down their formation. At the end of their lives these stars may have experienced supernovae explosions enriching their surrounding medium with heavier elements. Later, at  $z \sim 10$  the first galaxies formed taking advantage of the cooling from metals produced by stellar nucleosynthesis.

During the EoR, photons with energy greater than 13.6 eV photo-ionized almost all the intergalactic hydrogen, heating the IGM to thousands of degrees ( $10^4$  K) and producing an ionizing background that keeps the universe highly ionized at  $z < 6$ .

After that a final major phase transition happened, the HeII reionization, process that ended at  $z \sim 3$  and required a radiation field composed by  $h\nu > 54.6$  eV photons which heated the gas that gives rise to the Ly $\alpha$  forest. The high energy photons and the almost late end of this process, make the high redshift QSOs the best candidates to drive this phase of the universe. Moreover similarly to the hydrogen reionization, models predict a transition from a forest of HeII absorption lines at  $z \sim 2$  to the appearance of absorption at higher redshift.

Almost all our knowledge about the IGM comes from observations of distinct absorption features in the spectra of high-redshift QSO: the Ly $\alpha$  forest, the only direct evidence of the existence of the IGM and its properties.

### 2.3.1 The Ly $\alpha$ forest

The Lyman- $\alpha$  forest represents a plethora of absorption lines arising in the region blueward the Ly $\alpha$  of high redshift QSO spectra. It is due to several discrete systems at different redshift along the line of sight in which partially ionized hydrogen absorbs the radiation from the QSO. These absorbers consist of various intervening mass concentrations (outer edge of galaxies, halo gas, diffuse medium in the intergalactic space) that probably connect with each other to form the so-called cosmic web.

At first this phenomenon was observed with ground based telescopes in the optical range, being the Ly $\alpha$  line redshifted into this waveband for redshift  $z > 2$ .

In general, depending on the resolution of the observed spectra, the intergalactic absorbers can be fully described by three physical quantities: the redshift  $z$ , the HI column density and their line equivalent width (usually in terms of the Doppler parameter).

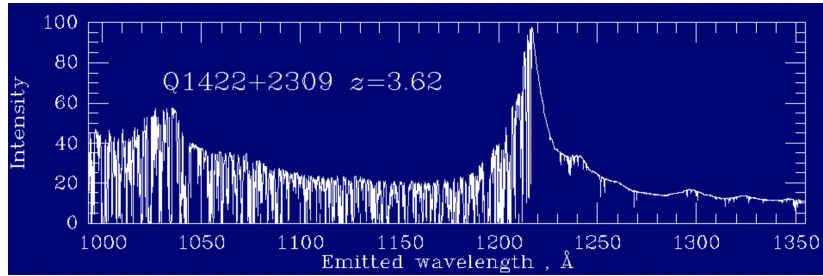


**Figure 2.5:** Spectrum of the Lyman $\alpha$  forest. On the blue side of the Ly $\alpha$  emission line, a large variety of narrow absorption lines of neutral hydrogen in the intergalactic medium is visible

In the Ly $\alpha$  forest we have that HI is discrete and not homogeneous, metal lines redward of the Ly $\alpha$  help securing the redshift of the absorbers and we have that is hard to identify stars associated to the absorbers since are too close to the QSO.

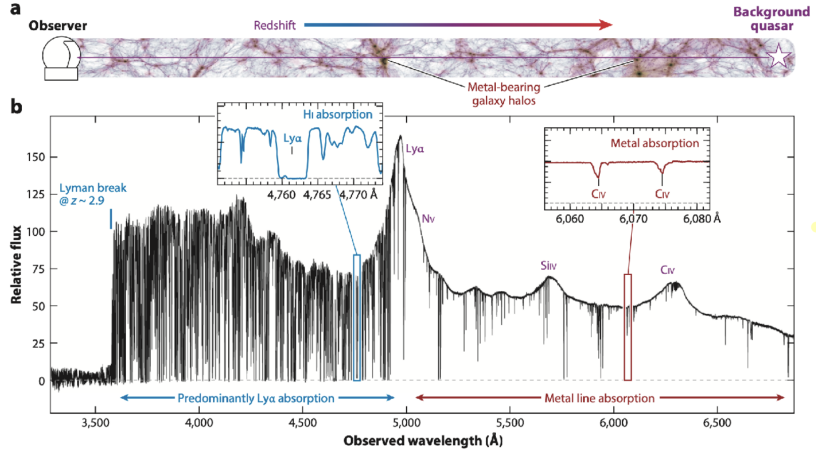


**Figure 2.6:** More on the Ly $\alpha$  forest

**Low spectral resolution** One of the methods used to infer statistical properties on the IGM is to measure the average depression (flux decrements) in the continuum of the spectra of distant sources (in the region shortwards of the Ly $\alpha$  emission) due to the presence of intervening Ly $\alpha$  and Ly $\beta$  absorption lines. When working in low resolution we are not able to see individual absorption.

The average flux decrement is defined as:

$$D_{A,B} = \left\langle 1 - \frac{F_{obs}}{F_{int}} \right\rangle_{A,B} \quad (2.16)$$

where  $A$  and  $B$  are wavelength ranges from Ly $\alpha$  to Ly $\beta$ , and Ly $\beta$  to Ly continuum (rest  $\lambda$  of 912 Å), respectively. In these measurements the fundamental source of uncertainty is the estimation of the true continuum level which is usually extrapolated from the region redward the Ly $\alpha$  in emission fitting some (unabsorbed) spectral windows with a power-law.

Measurements of the decrement at different redshift show a clear evolution of  $D_A$  and  $D_B$  with  $z$  due to the always higher presence of neutral hydrogen approaching the EoR.

**Intermediate spectral resolution** Increasing the spectral resolution it's possible to distinguish between the discrete absorption systems in the Ly $\alpha$  forest, therefore the distribution of the absorption lines in terms of equivalent width and redshift can be obtained.

It has been found that, for  $EW > 0.2$  Å this distribution follows an exponential trend:

$$\frac{\partial^2 N}{\partial EW \partial z} = \frac{N(z)}{EW^*} e^{-EW/EW^*} \quad (2.17)$$

where  $EW^* = 0.3$  Å and  $N(z)$  represent the redshift evolution of the line number density which goes as  $(1+z)^\gamma$  with  $\gamma$  depending on the type of absorber.

**High spectral resolution** In high resolution spectra we can resolve individual lines and study their line profile. Typically Voigt profiles are a good approximation of the line shapes, resulting from the convolution of different broadening mechanisms. In particular, considering a thermally broadened absorption line with the addition of a turbulence contribution, the Doppler parameter becomes:

$$\sigma = 2\sqrt{kT/m + b_{turb}^2} \quad (2.18)$$

where  $b_{turb}$  is the turbulent component of the Doppler parameter.

Observations show a gaussian distribution of the Doppler parameter with a peak between 25 and 30 km/s, a cut-off below 20 km/s and a dispersion of about 10 km/s. Assuming only thermal broadening this corresponds to an absorber temperature of  $\sim 2 \cdot 10^4$  K.

In Fig. 2.7 is shown the behavior of the equivalent width as a function of the  $N_{HI}$  column density, with a rapid rise at low values, a plateau when the core of the line reaches zero and a slow increase when the wings of the line start to erase the spectrum (line saturates, lorentzian profile, notice that we are working in a much wider range).

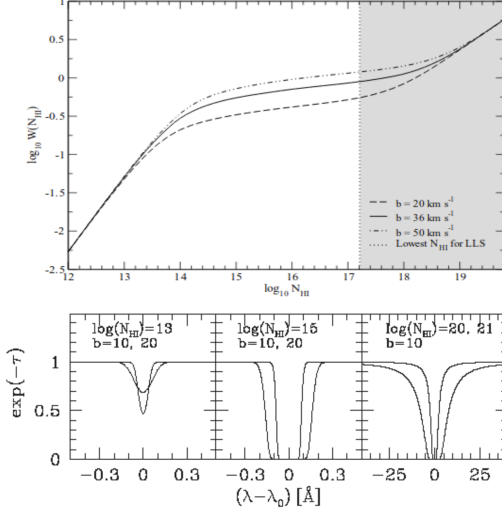


**Figure 2.7:** Curve of growth of the Ly $\alpha$  absorption line EW for different values of the Doppler parameter  $b$  ( $b = \sigma$ ). The shaded region indicates the characteristics LLSs column density (absorbers with  $N_{HI}$  corresponding to  $\tau = 1$  at the Lyman continuum at  $\lambda = 912\text{ \AA}$ ).

### 2.3.2 Absorption systems classification

Depending on the column density of the neutral hydrogen  $N_{HI}$  along the line of sight, the absorption systems are classified in different ways.

The Ly $\alpha$  forest presents the lowest HI column with  $\log_{10}(N_{HI}/\text{cm}^{-2}) < 17.2$ , these are called **Ly $\alpha$  systems**. Exceeding this limit the gas becomes optically thick to the ionizing radiation, creating a detectable discontinuity at the Lyman limit: these are the Lyman-limit systems (LLSs), lying in the range  $17.2 < \log_{10}(N_{HI}/\text{cm}^{-2}) < 20.3$ . At even higher column densities  $\log_{10}(N_{HI}/\text{cm}^{-2}) > 20.3$  the gas is almost completely self-shielded to ionizing photons, becoming predominantly neutral. These systems show the damping wing of the Ly $\alpha$  line and are therefore called Damped Ly $\alpha$  systems (DLAs).

To know the properties of a distant source, its spectrum has to be corrected for the absorption of these systems and in order to do it consistently we need an accurate model which describes the distribution of these absorbers along the line of sight. The evolution in redshift and density of the absorbing systems in the Universe can still be described by the **Madau model** (1995) in a simple and precise manner.

Assuming a random distribution of the absorbers, the mean optical depth along a line of sight at an observed wavelength  $\lambda_{obs}$  is:

$$\langle \tau_{\lambda_{obs}}^{IGM}(z_S) \rangle = \int_0^{z_s} \int_0^{\infty} \frac{\partial^2 N}{\partial z \partial N_{HI}} (1 - e^{-\tau_{abs}}) dN_{HI} dz \quad (2.19)$$

where  $z_s$  is the redshift of the source,  $\frac{\partial^2 N}{\partial z \partial N_{HI}}$  is the distribution function of the intergalactic absorbers and  $\tau_{abs} = \sigma_{\lambda_{obs}}^{HI} N_{HI}$  is the optical depth of an absorber with hydrogen column density  $N_{HI}$  at redshift  $z$  with HI cross-section  $\sigma$ . It is evident that an appropriate distribution function of the absorbers' number as well as time evolution is required to describe the intergalactic absorption.

The distribution function of intergalactic absorbers is defined as the number of absorbers along the line of sight per unit redshift interval and per unit HI column density interval. Usually a generic power-law redshift evolution independent of the HI column density is assumed:

$$\frac{\partial^2 N}{\partial z \partial N_{HI}} = A(1+z)^{\gamma} N_{HI}^{-\beta} \quad (2.20)$$

Given the rapid redshift evolution in  $1.8 < z < 3.8$  of the numerous optical thin clouds that compose the Ly $\alpha$  forest and the almost no evolution of the optically thick LLSs in  $0.7 < z < 3.6$  the distribution function is split into two parts:

$$\frac{\partial^2 N}{\partial z \partial N_{HI}} = \begin{cases} 2.4 \cdot 10^7 N_{HI}^{-1.5} (1+z)^{2.46} & \text{for } 2 \cdot 10^{12} < N_{HI}/\text{cm}^{-2} < 1.6 \cdot 10^{17} \\ 1.9 \cdot 10^8 N_{HI}^{-1.5} (1+z)^{0.68} & \text{for } 1.6 \cdot 10^{17} < N_{HI}/\text{cm}^{-2} < 2 \cdot 10^{20} \end{cases} \quad (2.21)$$

There is a break of the HI column density distribution around  $N_{HI} < 10^{17}\text{ cm}^{-2}$ , that can be seen in Fig. 2.8. This break arises around the threshold of LLSs, therefore is likely caused by the transition from optically thin to optically thick absorbers with respect to the ionizing radiation field.

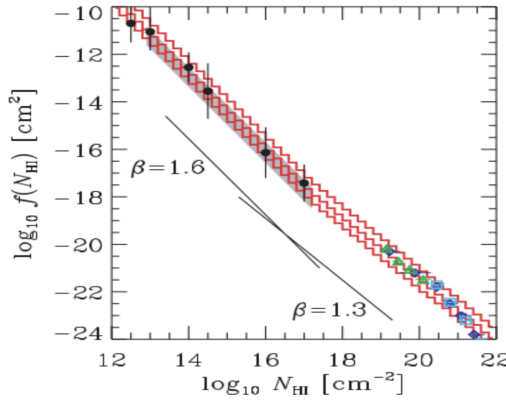


**Figure 2.8:** Distribution of the column density of absorbers along the line of sight. There is a slight change in slope.

Adopting the break at  $N_{HI} \simeq 10^{17} \text{ cm}^{-2}$ , a single redshift evolution can be assumed for all the absorbers independently of their column densities.

Integrating Eq. 2.19 we obtain the mean transmission function of the IGM. In Fig. ?? we have the typical staircase profile of the cosmic transmission for a source at  $z_S = 1, 3, 5$  (from top to bottom), obtained with different models.

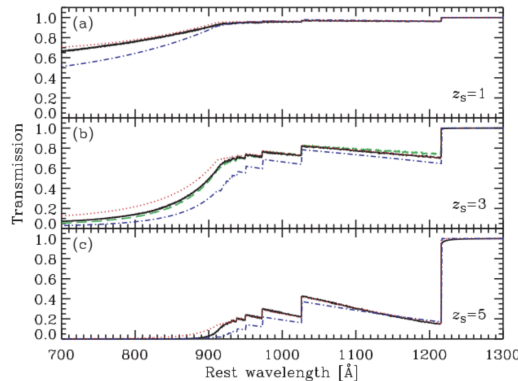


**Figure 2.9:** IGM transmissions obtained by integrating the Eq. 2.19 with a specific column density distribution of intergalactic absorbers for different models. The characteristic staircase profile (absorption of the Lyman series) is evident.

### 2.3.3 The cosmological UV background

Once the early re-ionization of HI was produced by the first sources (pop III stars) a question arises about how this ionization state would be maintained in the cosmic time. A second related question concerns the re-ionization of the He that requires high energy photons. What we need to know is the intensity of the cosmological UV background at different redshift.

The **ionizing ultraviolet background** is the diffuse radiation arising from QSOs/AGNs and young star forming galaxies (SFGs) and which is responsible to maintain the Universe in a highly ionized state. Its intensity and spectral shape are modulated by the sources driving the reionization process, therefore constraints on those features are of fundamental importance. An accurate study of the UVB is essential not only to get information on the IGM but also as input to cosmological hydrodynamics simulations.

### 2.3.4 Model for the reionization of the universe

The reionization process describes the balance between recombination and ionization in the universe. The transition from a neutral IGM to an almost fully ionized one (rate of LyC photon production is sufficiently high to balance the radiative recombination) can be fully described by the evolution with redshift of the dimensionless volume filling factor  $Q(z)$  (with  $Q = 1$  that implies that the reionization process is complete).

The high ionization threshold of helium, the small cross-section of HeII and the rapid recombination rate of HeIII delay this process at low redshift where is the activity peak of QSOs and AGNs (which produce hard UV photons). The time evolution of HII volume filling factor is:

$$\frac{dQ_{HII}}{dt} = \frac{n_{ion}}{\langle n_H \rangle} - \frac{Q_{HII}}{t_{rec}} \quad (2.22)$$

where  $\langle n_H \rangle = X_p \Omega_p \rho_c$  with  $X_p = 0.75$  corrects for the primeval helium fraction,  $t_{rec}$  the recombination time for hydrogen,  $n_{ion}$  the comoving number density of LyC photons ( $E > 13.6$  eV) per second that are able to reionize HI, expressed as:

$$n_{ion} = \int_{\nu_{HI}}^{\infty} \langle f_{esc} \rangle \frac{d\nu}{h\nu} \varepsilon_{\nu}(t) \quad (2.23)$$

with  $\langle f_{esc} \rangle$  the average escape fraction, i.e. the fraction of ionizing photons that escape from the ionizing source to affect the IGM and  $\varepsilon_{\nu}$  the emissivity in  $\text{erg s}^{-1} \text{Hz}^{-1} \text{Mpc}^{-3}$ .

In Eq. 2.22 if the first term on the right side wins the ionization is maintained while if the one winning is the second term the universe becomes neutral.

**Reionization from AGNs** Integrating this equation with the integral of Eq. 2.23 calculated for AGNs brings to the result in Fig. 2.10. In this way the hydrogen reionization turns out to be completed at  $z = 5.7$  (too late) while helium is doubly ionized at  $z = 4.2$  (too early). In particular this feature could be interpreted as a request for an abundant population of AGNs at this redshift which produce hard energy photons able to ionize He.

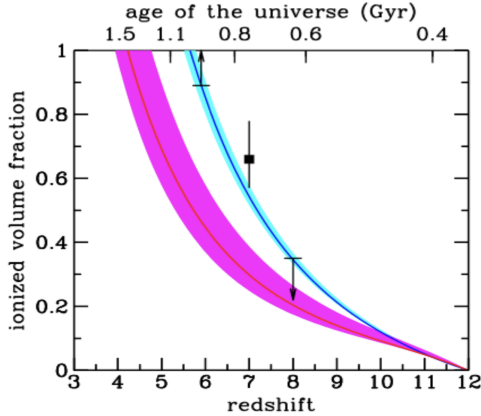


**Figure 2.10:** Reionization history of HII (blue) and HeIII (magenta) for an AGN-dominated scenario. Data points at  $z = 7$  and  $z = 8$  are the constraints on the neutral hydrogen fraction of the IGM inferred from the Ly $\alpha$  fraction in LGBs

**H reionization from galaxies** For a population of galaxies or quasars the volume density emissivity  $\varepsilon_{\nu}$  can be expressed integrating the observed luminosity function  $\Phi(L_{\nu}, z)$  as:

$$\varepsilon_{\nu} = \int_{L_{min}}^{\infty} L_{\nu} \Phi(L_{\nu}, z) dL_{\nu} \quad (2.24)$$

The luminosity function depends on the kind of sources responsible for the production of ionizing photons.

The existence of a decline in number density of bright QSOs and AGNs at  $z > 3$  has led to regard the high- $z$  SFGs as the most natural way of explaining the reionization of the universe (moreover emissivity of AGNs too low to keep the universe ionized).

The two critical parameters involved in the estimation of the contribution of SFGs to the reionization are the escape fraction of HI ionizing photons and the faint-end slope of the UV luminosity function. Estimations of the escape fractions of these galaxies are quite controversial both at low and high redshift.

## 2.4 The global baryon budget in absorption-line systems

The column density distribution of Ly $\alpha$  forest lines is a power-law. The relatively flat slope  $\beta \sim 1.6$  indicates that most of the neutral hydrogen is contained in systems of high column density.

To study the cosmic evolution of the density in condensed matter we can use the plot in Fig. ???. The total mass in baryons is inferred from cosmology  $\Omega_b = 0.043$  and is showed at the top. At all redshifts the neutral condensed gas density (DLAs, Ly $\alpha$  systems) dominates over that of the molecular gas. The molecular gas density is derived from sub-mm observations and its evolution roughly mirrors that of the star formation rate density hinting that the molecular gas reservoir drives the evolution of star formation. The star density is derived from galaxy survey. We see that there is an evident gap.

# Chapter 3

## Galaxy formation and evolution

For long time and even today detecting and characterizing galaxies at high redshift remains a significant challenge due to the effects of cosmological dimming of the surface brightness of extended objects ( $\propto (1+z)^{-4}$ ) and those of the K-correction that are particularly severe for the classical optical observations.

There are 5 main steps for a galaxy survey:

1. Selection
2. 3D distribution: redshift and distances
3. Physical properties: stellar mass, SFR, dust and gas content
4. Morphology
5. Dynamics

### 3.1 Selection

Selection is typically performed at some optical-NIR wavelength since optical telescopes have been for decades the most powerful instruments and stars shine mostly in the UV-optical-NIR. However in this way we might miss heavily dust-obscured galaxies!

### 3.2 Redshift-distance

We need efficient methods to select galaxies at different redshifts and epochs in the history of the universe. To go back in the past we need to go at high-z but surface brightness is dimming since:

$$B_{obs} = \frac{B_{em}}{(1+z)^4} \quad (3.1)$$

The main method is the **spectroscopic redshift**, typically using the emission lines since they do not require detecting the continuum. We have many emission lines in the optical rest-frame of star forming galaxies so we can use them in combination:

- $z = 0 - 1.5$ : OII detectable with optical spectroscopy
- $z = 2 - 6$ : with NIR spectroscopy

However if only one line is present in our spectra we cannot assign an unique  $z$ . Moreover, if we are working with passive galaxies we have that their optical rest-frame lacks emission lines therefore measuring their spectroscopic redshift is extremely difficult so we need longer integration times and identifying the absorption lines. If we try to observe in the NIR we have really bright skylines that are very difficult to cancel.

We can say that spectroscopic redshift is an expensive technique therefore we need to use other methods in order to identify the galaxies on which we should invest our observation time.

An idea would be performing a simple magnitude cut but in this way, although I can select deeper and deeper samples, a magnitude limited sample will always contain more nearby galaxies than distant ones. It is extremely inefficient!

Summarizing:

- light need to be dispersed vs wavelength and this is extremely time consuming
- with classical MOS spectrographs it is impossible to obtain spectra for all galaxies in a region of the sky at the same time
- it is the most precise technique since the error on the redshift is linked to the spectral resolution  $R = 1/\Delta\lambda$  so the ability of a spectrograph to deblend two lines separated by  $\Delta\lambda$
- it could be inaccurate, i can misinterpret a line for another one
- it is easier for star-forming galaxies that present emission lines than for passive galaxies than have only absorption lines

But how can we preselect objects that are likely at high redshift?

### 3.2.1 Narrow band technique

Narrow band filters can be used to identify bright lines in the spectra of galaxies at a specific redshift: for example a filter centered at  $\lambda_{obs} = 4670$  will contain the Lyman- $\alpha$  line for galaxies at  $z \sim 2.85$ . The galaxy that contains that emission line will be much brighter in this filter than in the other photometric bands. Different NB filters can be used to identify galaxies with Lyman- $\alpha$  at different redshifts allowing us to sample the whole history of the Universe.

This technique is also rather precise but sometimes is inaccurate as in principle we don't know what line causes the flux excess in the NB filter. Moreover is limited to narrow redshift intervals  $\Delta z$  so it does not cover large volumes of the universe and is biased towards objects with large/extreme EW, not corresponding to the typical population of galaxies.

### 3.2.2 Lyman Break galaxies

We need a technique that allows to explore the whole redshift range, covering large volumes of the universe: this technique involves the so-called Lyman break galaxies and uses wide-band photometry in multiple optical bands over large fields.

Since hydrogen is so abundant and its ionization cross section so large, one can expect that photons with  $\lambda < 912 \text{ \AA}$  are heavily absorbed by neutral hydrogen in its ground state inside the high- $z$  galaxy. Therefore, photons with  $\lambda < 912 \text{ \AA}$  have a low probability of escaping from the galaxy without being absorbed. Also intergalactic absorption contributes.

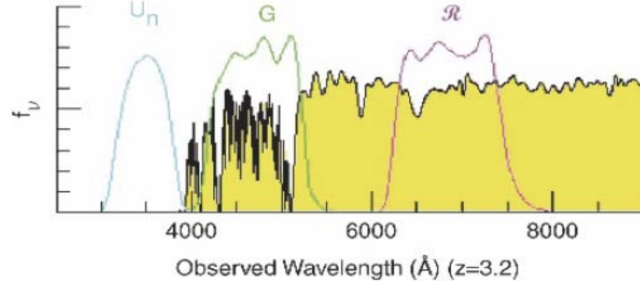


**Figure 3.1:** The flux below  $912 \text{ \AA}$  vanishes almost completely for  $z = 3.2$

So we have that all photons leftward of this limit are absorbed by the neutral hydrogen in the vicinity of the SF region: cleverly placing the photometric filters allows to identify the break at increasing redshift.

An example of this technique is represented in Fig. 3.2: in the first filter no light gets through as the bluer photons can not escape the galaxy at those wavelength while in the other two filters the galaxy is very bright (very star-forming so a lot of UV photons). Inverting the argument we can look in deep multi-band imaging of extragalactic fields galaxies that are dark in a filter and very bright in the two adjacent filters at larger wavelength.

Obviously the same filter combination is not effective at all redshift: at  $z = 3$  the best one is the UBV, at  $z = 4$  is BVI and at  $z = 5.5$  we choose RIZ.

**U-dropout** We talk about U-dropout when a galaxy disappears in the U band. It is a technique used to detect galaxies at  $z > 3$ : we consider three broad band filters with central wavelength  $\lambda_1 < \lambda_2 < \lambda_3$  with their spectral ranges chosen to not overlap. If  $\lambda_1 \leq (1+z)912 \text{ \AA} \leq \lambda_2$  a galaxy containing young stars should appear relatively blue

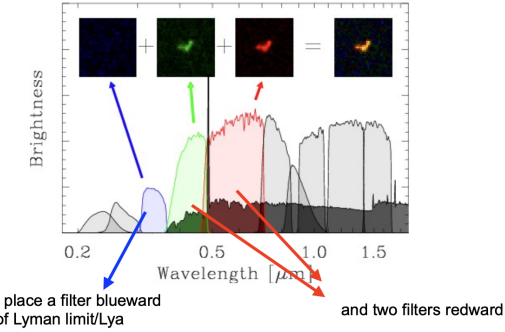


**Figure 3.2:** Example of application of the Lyman break method.

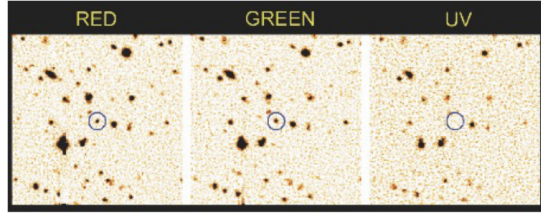


**Figure 3.3:** U-dropout: the galaxy disappears when observing in the U filter.

as measured with the filter  $\lambda_2$  and  $\lambda_3$  and be virtually invisible in the  $\lambda_1$  filter: because of the absorption it will drop out of this filter. For this reason galaxies detected in this way are called Lyman-break galaxies or Lyman drop-outs. This is explained using the UGR color-color diagram: the tracks in Fig. 3.4 are the colors that SED of different types of galaxies have at increasing redshift, starting from  $z = 0$  with  $\Delta z = 0.1$  steps. At  $z > 2.8$  the U-G color becomes very red for all types of galaxies (a consequence of the Ly $\alpha$  absorption in the intergalactic medium): the galaxy disappears from the U filter and at the same time the G-R color stays quite blue.

By using different filter sets drop-outs can also be discovered at larger wavelengths therefore higher redshift: for example this method has been applied up to  $z \sim 4.5$  yielding the so-called B drop-outs. However, candidates very high redshift galaxies detected as dropouts are very difficult to verify spectroscopically due to their very low flux.

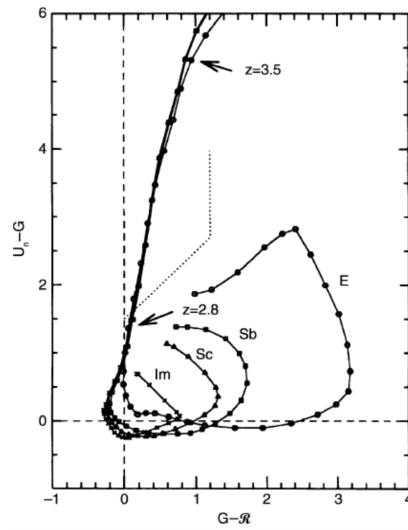


**Figure 3.4:** Evolutionary tracks in the (G-R)-(U-G) color-color diagram for different types of galaxies.

Summarizing we can say that this method is very **quick** (especially if compared with spectroscopic redshift) since we just need three very deep images to identify potential galaxies at given redshift. Moreover it is applicable to all galaxies in the field so we have an **high spatial coverage**. Unfortunately it is **less precise** than spectro-z since its precision depends on the depth of the Lyman break and on the width of the photometric filters and can be inaccurate since also the **dust** is responsible to make the colors redder simulating a break that is not there and also there is the possibility to confuse the Lyman break with the **Balmer break** (another discontinuity of the spectra at  $\lambda = 4000 \text{ Å}$ ). Finally this method is **biased** towards highly star forming galaxies.

### 3.2.3 Photometric redshift

A clear limitation in the LBG method rests on the fact that to properly work needs to assume that the intrinsic source spectra are those of young star-forming stellar populations mostly unaffected by dust extinction which obviously biases the selection. Therefore we need a new approach has been adopted that turned out to be valid for essentially all galaxy population and even for AGNs. This is the **photometric redshift method** that is a kind of extension of the color-color method used for the LBGs.

It is based on a grid of synthetic spectra of composite stellar populations that are fitted to multi-wavelength photometric data of a galaxy. This best-fitting process has to take into account also the displacement in wavelength due to the redshift, the K-correction, and the luminosity-distance relation. In this way the best-fit solution offers not only the stellar mass and average age of the galaxy but in particular a guess of the redshift.

So the spectral energy distribution of a galaxy is reconstructed over a wide wavelength interval, possibly from UV to nIR rest-frame. Then the SED is compared with a library of synthetic SED calculated at different redshift. This technique will be sensitive to the breaks in the SED (Lyman and Balmer), more in general will follow the SED shape constraining the photometric redshift.

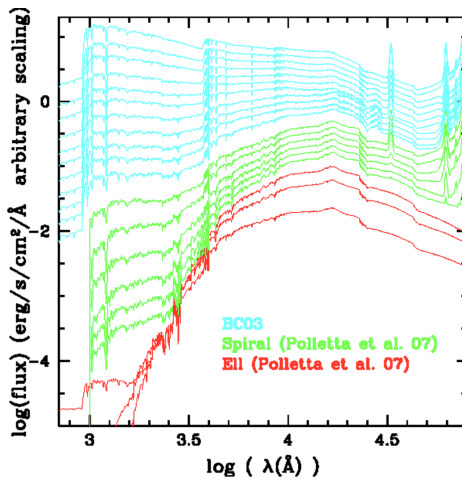


**Figure 3.5:** Synthetic SED at different redshift and morphological type

Also this method has advantages and disadvantages:

- is faster if compared to spectroscopic redshift since we need only deep photometry in some bands is needed
- works for all galaxies in a survey so it has an high spatial completeness
- since is sensitive to the global shape of the SED, is more accurate and precise than the Lyman break technique
- we have a degeneracy between dust content (and age) and redshift since both make the SED redder
- works only if the SED breaks (Lyman and Balmer) are covered by photometry and are very deep

In order to calibrate the photometric redshift, the measurements are compared with spectro-z. In this phase, sophisticated iterative training and machine learning techniques are used: photometric redshifts are modified until they match the spectro-z ones.

In the end all the different techniques to select galaxies and constrain their redshift are **used together**:

1. In a given area of the sky deep images in many photometric bands going from the UV to the nIR rest-frame are obtained;
2. SEDs for each objects in the field are built;
3. Photo-z are determined for each galaxy;
4. The Lyman Break technique is used to select the most distant galaxies;
5. Through spectroscopy spectra are obtained and spectroscopic redshift are measured for specific subsamples of galaxies;

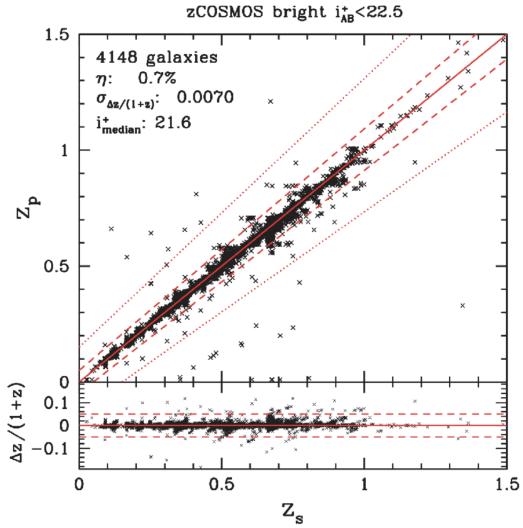


**Figure 3.6:** Photometric redshift versus spectroscopic redshift, calibration.

6. These spectro-z are used to improve LBG and photo-z selections.

Then, once accurate redshifts are measured, we can distribute galaxies in **distance** and **lookback time**.

### 3.3 Physical properties at zero redshift

Once redshift and distance are assigned to each galaxy, the physical parameters are determined: stellar masses, star-formation rates, stellar population age, metallicity, dust and gas content...

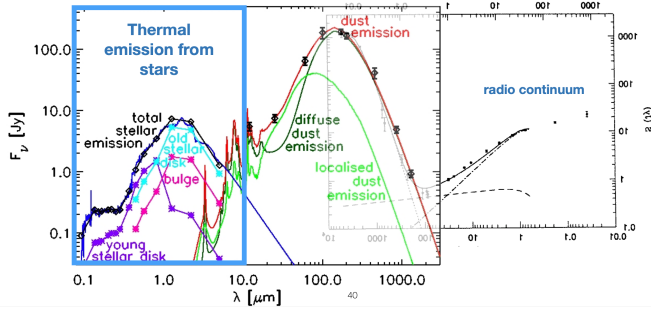


**Figure 3.7:** SED of galaxies: the light in the UV/optical is absorbed by dust and then re-emitted in the FIR.

#### 3.3.1 Stellar population synthesis

Light from galaxies comes from the stars and the spectral radiation of stars can be calculated with the theory of stellar atmospheres. If the distribution of the number density of stars as a function of their mass is known we can calculate the total light emitted by them.

The theory of **stellar population synthesis** aims at interpreting the spectrum of galaxies as a superimposition of stellar spectra. Taking into account the fact that the distribution of stars changes over time (massive stars leave the main sequence so the number of luminous blue stars decreases and the spectral distribution of the population changes) we can say that the spectral energy distribution of a galaxy reflect its history of star formation and stellar evolution. For this reason simulating different star formation histories and comparing them with the observed galaxy spectra provides important clues for understanding the evolution of galaxies.

#### 3.3.2 Initial mass function

The IMF tells us the mass distribution of stars for a stellar population at its birth. It is estimated by counting stars of various spectral type in young environments, rich in O and B stars. Its study is limited to the solar neighborhood

and to some very close galaxies like the Magellanic clouds. The IMF is not universal, there are different functions. The most famous one is the **Salpeter IMF** for which:

$$\phi(m) \propto m^{-2.35} \quad (3.2)$$

This IMF seems to be a good description for stars with  $M \geq 1 M_{\odot}$ , whereas the IMF for less massive stars is flatter. Two other frequently used IMFs are the Chabrier and the Kroupa, which have a similar slope and different cut-off at low masses. However these functions are subject to revision at very high-z to match JWST results.

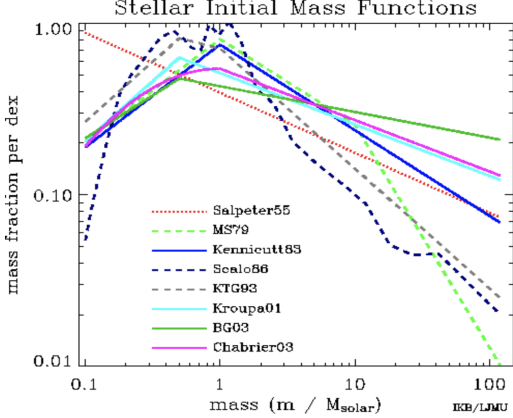


**Figure 3.8:** Various IMFs, detailing the probability distribution of stellar masses at formation. The normalization is arbitrary and the reference distribution is the Salpeter one.

### 3.3.3 Single stellar populations

The starting point of any SPS model is the single stellar population which describes the evolution in time of the SED of a single, coeval stellar population at a single metallicity and abundance pattern. An SSP requires three basic inputs: stellar evolution theory in the form of isochrones, stellar spectral libraries and an IMF. These components are then combined in the following way:

$$F_{\lambda}(t, Z) = \int_{M_l}^{M_u} f_{\lambda}(M, t, Z) \phi(M) dM \quad (3.3)$$

where  $M$  is the initial stellar mass (ZAMS),  $\phi(M)$  is the initial mass function,  $f_{\lambda}$  is a stellar spectrum and  $F_{\lambda}(t, Z)$  is the resulting time and metallicity dependent SSP spectrum. The lower limit of integration is typically taken to be the hydrogen burning limit  $0.08 M_{\odot}$  and the upper limit is dictated by stellar evolution.

In order to compute  $f_{\lambda}$ , models for stellar evolution and stellar atmospheres are needed. For what regards the age of the stellar population we can simply use an **isochrone**: the number density of stars along an isochrone depends on the IMF and the spectrum is the sum over all spectra of the stars on an isochrone.

The SED of SSP can evolve over time: the more massive and blue stars gradually leave the main sequence and turn red then disappear and the total luminosity decreases, therefore SSP SEDs become redder and redder as they age.

Of particular importance is the spectral break located at about 4000 Å which becomes visible in the spectrum after a few  $10^7$  yr. This break is caused by a strongly changing opacity of the stellar atmospheres at this wavelength due to strong transitions of singly ionized calcium and the Balmer lines of hydrogen. The 4000 Å break is one of the most important spectral properties of the continuum stellar emission in galaxies.

### 3.3.4 Composite stellar populations

Real galaxies are systems made of stars with different ages therefore we need to sum together stellar populations with different ages and their spectral distribution is mainly determined by the ratio of the star formation rate today to the mean star formation rate in the past.

Composite stellar populations differ from the simple ones in three aspects: they contain stars with a range of ages, of metallicities and contain dust.

We start hypothesizing a star formation history for each type of galaxy: ellipticals have almost all very old stars, spirals have old and young stars and Sd spirals form stars in a constant manner. Then SEDs of SSPs of different ages are added together: each age has a weight that depends on the form of the star formation history of that composite population. In this way it is possible to build practically infinite combinations of SEDs of galaxies, with more or less old populations than young ones.

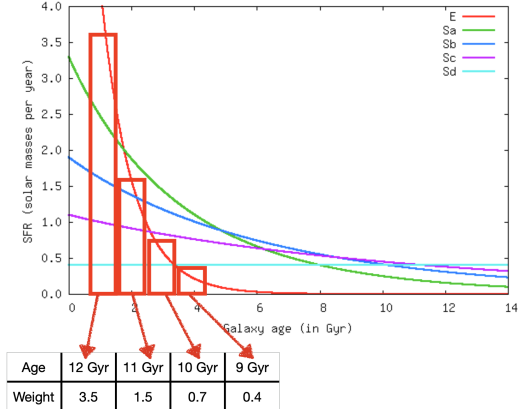


**Figure 3.9:** The colored solid lines represent the SFH for different morphological types, the red squares are different stellar populations with different ages and weights. In this case we are trying to build a CSP for an elliptical galaxy.

### 3.3.5 The spectra of galaxies

Through multi-band photometry we can obtain the SED of real galaxies and we compare it with the SED of SSPs, obtaining in this way the total number of stars, the total mass in stars ( $M^*$ ) and the number of young stars. All these ingredients compose the SFR: how many stars are forming at a specific moment per unit of time.

If we look at the typical spectra of various types of galaxies (Fig. 3.10) we see that it is easy to recognize a general trend: the latter the Hubble type, the bluer the overall spectral distribution, the stronger the emission lines, the weaker the absorption lines and the smaller the 4000 Å break.

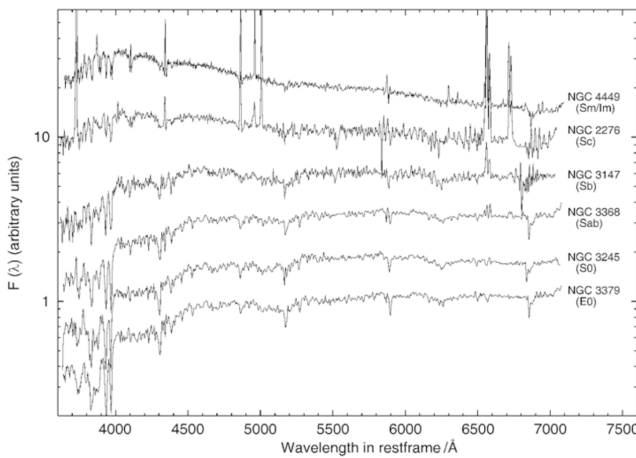


**Figure 3.10:** Spectra of galaxies of different type where the spectral flux is plotted logarithmically in different units. The spectra are ordered according to the Hubble sequence with early types at the bottom and late-type spectra at the top.

Therefore we have:

- **spiral galaxies:** blue spectra (slope  $< 0$ ) and many emission lines – young galaxies with ongoing star formation
- **elliptical galaxies:** red spectra (slope  $> 0$ ) and no emission lines – old galaxies with no SF

In Fig. 3.11 we compare the SED of different types of galaxies. In blue we have **ULIRG** (Ultra Luminous InfraRed Galaxies), the most luminous galaxies in the universe. In red we have **starburst** galaxies which are typically irregular with many young stars and ongoing star-formation. Then in violet we have **disks**, which are the typical spiral galaxies which present a moderate SFR. Finally in green the **elliptical** galaxies with no ongoing star formation and very little

dust. The shape of the different SEDs is quite similar so, in order to reduce age-dust-z degeneracy we need some information on the dust amount.

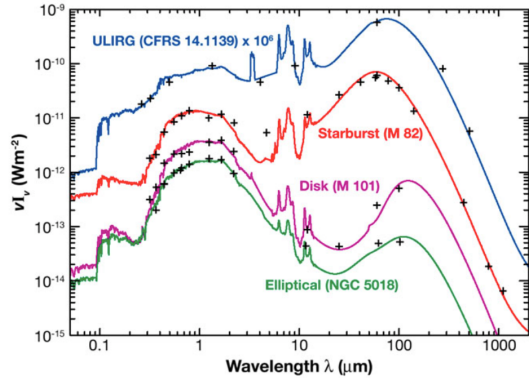


**Figure 3.11:** Comparison of different SEDs.

### 3.3.6 ISM components

The interplay between gas, dust and stars determine the evolution of galaxies but how do we study ISM and dust in distant galaxies?

The major ISM components are:

- Gas - interstellar hydrogen that may be neutral (HI, 100 K), molecular ( $\text{H}_2$ , 50 K) or ionized (HII,  $10^4$  K);
- Dust - silicates and graphite (10-20 K, up to 50 K at high-z)

The HI can be observed using the 21 cm line in absorption ( $\text{Li}\alpha$ ) or in emission. For what concerns the molecular gas we have that  $\text{H}_2$  is the most common molecule and the fuel for star formation but however is virtually invisible since it has no dipole moment so it does not emit. CO is the second most common molecule, observable in sub-mm for example using ALMA and is used to trace the  $\text{H}_2$ .

The ionized gas HII is produced by hot stars that, ionizing the surrounding gas produce the so-called HII regions. Dust is one of the responsible for the change in color of a stellar population: in fact it absorb the light from hot stars, re-emitting the energy as black body radiation with  $T \sim 30$  K. Is more efficient at short wavelength. Looking at Fig. 3.11 we can distinguish between two regions: the one leftward the central spikes is the region where we have dust extinction while the one rightward is the one where we have thermal dust emission.

The dust can be studied using ALMA in the millimetric and sub-mm both in spectroscopy and photometry. In fact using spectroscopy we can study the sub-mm lines that allows to study the physical state of the ISM, star-formation, gas mass and kinematics, while using photometry we can study the dust emission and therefore the obscured star formation and the dust/gas content.

### 3.3.7 Morphology

The most used classification scheme is the Hubble one according to which three main types of galaxies exist:

- **Elliptical galaxies** – nearly elliptical isophotes without any clearly defined structure;
- **Spiral galaxies** – disk with spiral arm structure and a central bulge, divided into two sub-categories: normal and barred;
- **Irregular galaxies** - galaxies with only weak or no regular structure;
- **S0 galaxies** – transition between ellipticals and spirals which are also called lenticulars as they are lentil-shaped galaxies.

These morphological classes are based on a visual analysis but obviously correlate with many observed properties: color bimodality, stellar mass and age, dynamics and many more.

Talking about **bimodality** we have that if we try to classify galaxies using their color (photometric measurements mostly) and plot their density distribution into a color-magnitude diagram, we have two density peaks: one at high luminosity and red color and one at fainter magnitudes and bluer color. These are the red sequence and the blue cloud and in between them we have the green valley.

**Visual analysis** The first way to classify galaxies is analyzing them visually. Unfortunately the eye is not very objective and it is difficult to classify by eye the hundreds thousand galaxies in modern surveys.

**Light profiles** Another way is using the surface brightness profile as the Sérsic profile (generalization of the deVaucouleurs one):

$$\mu(r) \propto r^{-1/n} \quad (3.4)$$

where  $\mu(r)$  is the surface brightness profile,  $n$  the Sérsic index that if is equal to one we have an exponential profile (a disk) and if it is equal to 4 we have a deVaucouleurs profile (bulge or elliptical). The Sérsic index correlates with the morphological class: a large  $n$  indicates a galaxy dominated by the bulge while a small  $n$  indicates a disk dominated galaxy. Therefore, in principle, we can use  $n$  to automatically classify galaxies.

A program that uses this approach is GALFIT, an automatic tool to analyze 2d profiles. This algorithm gets in input the galaxy image, the PSF image and some initial guesses for the parameters and in a few seconds gives in output the image for the model, the residual image, the position, magnitude, radius, b/a, PA for each component.

**Non-parametric methods** Another kind of automatic classification is the one for imaging that uses various parameters that can be computed using and manipulating the images of galaxies as **asymmetry**, the **clumpiness** and the **concentration**. This method do not need any assumption on the light distribution so it is better adaptable to all kind of galaxies.

Using the CAS parameters and plotting the galaxies in the C-A or S-A planes we see that there is a region where preferentially elliptical galaxies are located: however that region suffers for some degree of contamination since there are some spirals within it. To divide the two populations we can either draw the lines dividing them by eye or we can use Machine Learning techniques as for example clustering k-means to separate classes automatically based on a set of observable and a control sample.

Applying the CAS classification at various redshift we find an interesting result: there are passive elliptical galaxies at all redshifts.

### 3.3.8 Dynamics

The dynamics of galaxies can be studied through spectroscopy. One method is using integral field spectroscopy for which we can obtain a spectrum for each spatial *spaxel*, lowering the time spent for the observations. We can obtain a spectrum for each position in the image or an image for each wavelength.

We can use a single line, i.e. H $\alpha$  to map the velocity of different regions of a galaxy, therefore mapping the velocity field, once the systemic velocity has been subtracted.

## 3.4 Physical properties at high redshift

### 3.4.1 Morphology

Morphology of high redshift galaxies can be revealed easily with HST and JWST: some galaxies are similar to the ones in the Hubble morphological sequence, other have very peculiar morphologies which are uncommon in the local Universe. Therefore we have an interesting result: at high redshift we can use the same classes in the morphological diagram but we also have to add some new classes.

Local galaxies can be classified according to their color, with most of them being either member of the red sequence or the blue cloud with a tight correspondence between the Hubble classification and the galaxy color and morphological parameters (Sérsic index).

However at high redshift ( $z > 3$ ) the most of the galaxy are **star forming** and mostly **irregular** or **clumpy**, not falling in the Hubble sequence. These clumps are typically bluer than the rest of the galaxy, hence their star population has a younger age than the underlying disk.

Quiescent galaxies become more abundant towards lower redshift. For  $z > 2$  peculiar galaxies dominate the galaxy population with some quiescent, spheroidal galaxies already present but a negligible disk population. At  $z \sim 2$ , the abundance of spheroidal and disk galaxies together starts to overtake the peculiar population, where this redshift depends on mass: at higher mass the fraction of Hubble sequence like galaxies is higher than at lower masses indicating

that they finish their morphological evolution earlier. Thus starting from  $z \sim 2$ , the Hubble sequence is gradually built up.

Today, thanks to JWST we are able to reveal for the first time the optical rest-frame morphology of galaxies at  $z > 3$ .

As we have already said the color distribution at high- $z$  is bimodal like in the local universe and galaxy properties still correlate with the morphological classification.

### 3.4.2 Star formation

**Star-forming main sequence** If we plot local galaxies in a mass vs SFR plane we see that they lie in specific sequences.



**Figure 3.12:** Local galaxies distributed in a mass vd SFR plane.

We have the **main sequence** (the blue cloud) in which the bulk of the galaxies lie on a very tight relation: more massive galaxies form stars more rapidly. Then we have **starburst galaxies** that form stars much faster than normal galaxies of the same mass. On the lower part we have **passive galaxies** (the red sequence) which are dead galaxies that do not form new stars anymore and then the **green valley** in which there are galaxies that are intermediate between the main sequence and passive galaxies.

**Starburst galaxies** Starburst galaxies are characterized by a strongly enhanced star formation rate, compared to normal galaxies. According to the general consensus they are prevalently mergers, collision of galaxies in which gas is driven to the center of the systems therefore triggering new star formation.

Collision of galaxies are spectacular events that take place over hundreds of millions of years, such events must have been more frequent in the distant past when the universe was smaller and galaxies were closer. Observations confirm that distorted looking galaxies, likely ongoing galactic collisions, were more common in the early universe than they are today. Moreover collision is one of the channels through which elliptical galaxies can form but is not the only one and possibly not even the dominating one.

**Evolution of the main sequence** Even at high- $z$  galaxies follows the same main-sequence and its slope remains more or less constant. What changes is the normalization: galaxies at increasing redshift form stars more efficiently, galaxies were forming stars more rapidly in the past.

### 3.4.3 Galaxy luminosity function

The most convenient way to analyze the light coming from galaxies is using the luminosity function in different bands in terms of a fit with a Schechter function:

$$\phi(L) = \left(\frac{\phi^*}{L^*}\right) \left(\frac{L}{L^*}\right)^\alpha \exp(-L/L^*) \quad (3.5)$$

**The UV luminosity function** The LF measured in the UV band can trace the star formation rate since the most luminous sources of UV light are the star forming regions. The overall abundance of UV-luminous galaxies is considerably larger in the redshift interval  $2 \leq z \leq 4$  than it is today therefore in that period the star formation rate was higher. Going at even higher redshift the abundance of UV-luminous galaxies decreases again, moreover for these very high redshifts most of the luminosity in the UV is emitted from faint sources.

Integrating the UV luminosity function at each redshift we obtain the number density of new stars formed in the universe at each epoch: the **star formation rate density**. Using this we can build the Lilly-Madau diagram in which we have the SFR as a function of the redshift. From this plot we see that the universe was much more efficient in forming stars 10 billion years ago and that most of the stars in the universe were formed between 8 and 11.5 billion years ago.

**Mid-IR luminosity function** Whereas the rest frame UV radiation indicates the level of star formation which is unobscured by dust, it misses those star forming galaxies which are heavily obscured by dust. Their activity can be best seen in the rest-frame mid and far IR. Therefore the most reliable indicator of the obscured star formation rate is the bolometric infrared luminosity.

In the **K band** the emission is dominated by K and M stars which dominates even the mass budget of galaxies. We can therefore determine the stellar mass function: the distribution of galaxies as a function of stellar mass.

The main problem of observation in these bands (far-IR and sub-mm) is the identification process: in fact most of the time the counterparts are very faint optical galaxies, almost invisible, so their spectroscopic analysis is difficult. For this reason although relative large samples of far-IR and sub-mm galaxies were made available by the various observatories both on from space and ground, their physical characterization was clearly difficult.

### 3.4.4 Evolution of the mass function

Near-IR luminosity of galaxies offer an excellent proxy of their stellar mass because this mass is dominated by low-mass stars, whose low photospheric temperature contributes mostly to the near-IR integrated light of a galaxy. Hence if we calculate the M/L ratio between the stellar mass of a galaxy and its K-band near-IR luminosity we can immediately convert the near-IR K-band luminosity functions into stellar mass functions.

The evolution of the stellar mass function gives information on the assembly history of galaxies so when they assemble their mass. Comparing the history of star formation with the observations we have that the most massive galaxies are the first to assemble their stellar mass while the less massive ones assemble on a larger timescale.

The consequence is that elliptical galaxies can not be formed mainly through merging of spiral galaxies.

## 3.5 Super massive black holes

Active galactic nuclei are supermassive BH in the center of galaxies that are very bright at different wavelengths (X-ray, optical, IR and/or radio). The mass of the central BH can be calculated from the orbits of the molecular clouds around it. Knowing the mass of the central BH we have a linear relation between the BH mass and the galaxy stellar mass that can therefore be easily computed.

This correlation indicates a link between the growth of galaxies and that of the central black hole: if one grows so does the other. Galaxies are affected by the black hole and they affect it in a process called **feedback**. In addition when the black hole is active it heats the surrounding gas preventing new star formation and can even fire jets of gas intergalactic distances: **black holes regulate the star formation rate in galaxies**.

# Appendix A

## Lyman- $\alpha$ based techniques

### A.1 Damped Lyman- $\alpha$ systems (DLA)

First important attempt to identify high-redshift galaxies by exploiting spectroscopic observations of high-redshift quasars to detect neutral hydrogen present in primeval galaxies looking for the absorption features in bright quasar spectra. The absorption feature would concern the Lyman- $\alpha$  line due to neutral hydrogen in galaxies, hence detected as deep absorption shortward the quasar Ly $\alpha$  emission line.

DLAs may represent condensations of gas that turn into "normal" galaxies once star formation settles in. This interpretation is supported by the kinematical properties of DLAs. Whereas the fact that the Ly $\alpha$  line is damped implies that its observed shape is essentially independent of the doppler motion velocities of the gas.

Every DLA is associated with metal absorption lines systems covering low and high ionization species. The profiles of these metal lines are usually split up into several components. These components are interpreted as ionized clouds whose velocity range can be used as an indicator of the characteristic velocities of the gas in the DLA: the observed distributions are compatible with the interpretation that DLAs are rotating disks with a characteristic rotational velocity of  $v_r \sim 200$  km/s.

If the interpretation is correct we expect that DLAs can be also observed as galaxies in emission. However this is impossible for high-redshift galaxies since we need extremely high resolution.

For DLAs at low redshifts the observational situation is different since a fair fraction of these systems have counterparts seen in emission. It seems that the low-redshift population of DLAs may be composed of normal spiral galaxies.

For DLAs is relatively easy to measure their heavy metal content from the metal lines associated to Ly $\alpha$ . These are typically only one tenth of the solar metallicity proving that these objects have still to experience their main phases of star formation.

### A.2 Lyman- $\alpha$ emitters and blobs (LAEs)

One of the oldest methods to discover high-redshift galaxies is based on the use of narrow-band photometric imaging on wide fields to detect objects with prominent emission lines. This technique has been used extensively to search for Lyman- $\alpha$  emitters at redshift  $z > 3$  for which the Ly $\alpha$  emission line ( $\lambda = 1216$  Å) appears in the optical.

Objects with strong Ly $\alpha$  are either QSOs or galaxies actively forming stars, however since the Ly $\alpha$  flux is easily quenched by dust extinction, not all star forming galaxies show Ly $\alpha$  emission. Therefore, by selecting LAEs one is biased towards star-forming galaxies with relatively low dust.

One can search for LAEs at a particular redshift using a narrow-band filter centered on a wavelength  $\lambda = 1216 \cdot (1+z)$  plus another much broader filter centered on the same  $\lambda$ . The object in question then will appear particularly bright in the narrow-band filter in comparison to the broad-band image. Another problem is that one might also select emission-line galaxies at very different redshift (i.e. [OIII] emission): to minimize this kind of contamination one generally only selects systems with large equivalent width in the emission line ( $\sim 150$  Å).

Another method to check whether the object is indeed a LAE is to use follow-up spectroscopy to see if there are any other emission line visible that help to determine the redshift and if the emission line is asymmetric as expected for Ly $\alpha$  due to preferential absorption in the blue wing.

This technique has been used to search for high-redshift galaxies in several narrow redshift bins ranging from  $z \sim 3$  to  $z \sim 6.5$ . The evolution of LAEs with redshift is a direct probe of the Ly $\alpha$  transmission of the IGM.

### A.2.1 Lyman- $\alpha$ blobs

The search with narrow band imaging has revealed a class of objects which are called Ly $\alpha$  blobs: these are luminous and extended sources of Ly $\alpha$  emission, their characteristic flux in the Ly $\alpha$  line is  $\sim 10^{44}$  erg/s. The nature of these high-redshift objects is currently unknown.